The DOI for this manuscript is doi: 10.1175/JCLI-D-15-0511.1

Révelard, A., C. Frankignoul, N. Sennéchael, Y. Kwon, and B. Qiu, 2015: Influence of the decadal variability of the Kuroshio Extension on the atmospheric circulation in the cold season. J. Climate. doi:10.1175/JCLI-D-15-0511.1, in press.

Influence of the decadal variability of the Kuroshio Extension on the atmospheric circulation in the cold season

Adèle Révelard[1], Claude Frankignoul and Nathalie Sennéchael

Sorbonne Universités (UPMC, Univ. Paris 06) CNRS/IRD/MNHN, LOCEAN/IPSL, Paris, France

Young-Oh Kwon

Woods Hole Oceanographic Institution, Woods Hole, Massachusetts

Bo Qiu

Department of Oceanography, University of Hawaii at Manoa, Honolulu, HI, USA

Submitted to Journal of climate

July 18, 2015

[1] *Corresponding author address:* Adèle Révelard, LOCEAN/IPSL, Université Pierre et Marie Curie, 4 Place Jussieu, 75252 Paris Cedex 05, France
E-mail: arlod@locean-ipsl.upmc.fr

Abstract

The atmospheric response to the Kuroshio Extension (KE) variability during 1979-2012 is investigated using a KE index derived from sea surface height measurements and an eddy-resolving ocean general circulation model hindcast. When the index is positive, the KE is in the stable state, strengthened and shifted northward, with lower eddy kinetic energy, and the Kuroshio Oyashio Extension (KOE) region is anomalously warm. The reverse holds when the index is negative. Regression analysis shows that there is a coherent atmospheric response to the decadal KE fluctuations between October and January. The KOE warming generates an upward surface heat flux that leads to local ascending motions and a northeastward shift of the zones of maximum baroclinicity, eddy heat and moisture fluxes, and the storm track. The atmospheric response consists of an equivalent barotropic large-scale signal, with a downstream high and a low over the Arctic. The heating and transient eddy anomalies excite stationary Rossby waves that propagate the signal poleward and eastward. There is a warming typically exceeding 0.6 K at 900 hPa over eastern Asia and western United States, which reduces the snow cover by 4 to 6%. One month later, in November-December-January-February, a high appears over northwestern Europe, and the hemispheric teleconnection bears some similarity with the Arctic Oscillation. Composite analysis shows that the atmospheric response primarily occurs during the stable state of the KE, while no evidence of a significant large-scale atmospheric response is found in the unstable state. Arguments are given to explain this strong asymmetry.

1. Introduction

The Kuroshio Extension (KE) is an eastward flowing inertial jet extending the western boundary current of the North Pacific subtropical gyre after it separates from the Japan coast. It is accompanied by large-amplitude meanders and energetic pinch-off eddies (e.g., Qiu and Chen 2005; Kelly et al. 2010). Its path is well defined by the maximum meridional gradient of the sea surface height (SSH), which is located near 35°N. This is south of the North Pacific subarctic frontal zone (SAFZ) associated with the Oyashio Extension (OE), an extension of the western subarctic gyre, which is defined by the maximum meridional sea surface temperature (SST) gradient and found somewhat north of 40°N. The two currents have a different vertical temperature structure as the KE front is strongest between 200 and 600 m but has a modest SST gradient, while the OE is shallow and has a strong SST gradient (Nonaka et al. 2006).

The KE system exhibits large decadal fluctuations between relatively stable and unstable states (Qiu and Chen 2005, 2010; Taguchi et al. 2007; Qiu et al. 2014). When in the stable state, the KE jet is strengthened, its path is shifted northward, the regional eddy kinetic energy is lower, and the southern recirculation gyre intensified. The reverse holds in the unstable state. Previous studies have shown that the KE responds to basin-scale wind forcing over the central North Pacific with a delay of 3 to 4 years linked to baroclinic Rossby wave propagation (e.g. Seager et al. 2001; Schneider et al. 2002), and that frontal-scale inertial fluctuations initiated by the arrival of the Rossby waves narrow the KE jet (Taguchi et al. 2007; Sasaki et al. 2013). Qiu (2003) suggested that the SSH in the KE region is mainly driven by fluctuations in the strength and location of the Aleutian low, while Ceballos et al. (2009) argued that the main driver of the KE strength change was the North Pacific Oscillation, although the two modes are not well separated in the satellite altimetry era (Qiu and Chen 2010), nor in the period considered in the present paper. On the other hand, the

93 transport and meridional position of the OE respond rapidly to the wind stress changes
94 associated with the Aleutian low via barotropic Rossby wave propagation and Ekman currents,
95 while being also remotely forced near 160°-170°E about 3 years before (e.g., Qiu 2002;
96 Nonaka et al. 2008). Hence, the decadal variability of the KE and the OE is not necessarily
97 coherent (Nonaka et al. 2006). Frankignoul et al. (2011b, hereafter FSKA) indeed found
98 negligible correlation between their KE and OE indices.

99 The Kuroshio-Oyashio Extension (KOE) region is an area of maximum heat release
100 from the ocean to the atmosphere and strong interannual SST variability, especially on its
101 northern side along the OE (Kelly et al. 2010; Kwon et al. 2010). Vivier et al. (2002) showed
102 that interannual changes in the upper ocean heat content of the KE are dominated by
103 geostrophic advection, with a clear signature in SST. Sugimoto and Hanawa (2011) showed
104 that SST changes are primarily responsible for turbulent heat flux variations. Because of the
105 strong ocean-to-atmosphere fluxes of heat and moisture, the KOE is a region of large
106 cyclogenesis, as major storm tracks are organized along or just downstream of the main
107 oceanic frontal zones (Hoskins and Hodges 2002; Bengtsson et al. 2006). Nakamura et al.
108 (2004) and Taguchi et al. (2009) have argued that differential heat supply across the North
109 Pacific SAFZ acts to maintain surface baroclinicity, sustaining storm development and the
110 anchoring effect of the SST frontal zones, and they suggested that their variations may affect
111 storm track activity and the westerly jets.

112 Observational evidence that North Pacific SST anomalies influence the large-scale
113 atmospheric circulation has been found in several studies, based on its relation with preceding
114 SST fluctuations (Liu et al. 2006; Frankignoul and Sennéchael 2007; Wen et al. 2010;
115 Taguchi et al. 2012; Gan and Wu 2013). Modeling studies have also documented the ocean-
116 to-atmosphere feedback in the KOE region (Peng and Whitaker 1999; Kushnir et al. 2002;
117 Liu and Wu 2004; Gan and Wu 2012; Smirnov et al. 2015). These experiments suggest that

the atmospheric response is primarily governed by nonlinear transient eddy feedbacks, which act both to amplify the downstream response and make it equivalent barotropic. It is sensitive to the mean background flow, and consequently to the season considered. Smirnov et al. (2015) focused on the local atmospheric response to an Oyashio frontal shift by prescribing in a high-resolution AGCM the corresponding SST anomaly. The others used a basin-wide SST pattern centered in the KOE region, and the possible links with the variability of the western boundary current extensions were not investigated. However, Joyce et al. (2009) found that the year-to-year shifts in the KE path were followed by significant changes in the near-surface synoptic activity, and FSKA suggested that the meridional shifts of the KE during 1980-2006 had a significant impact on the large-scale atmospheric circulation, as a northward shift of the KE was primarily followed by high pressure anomalies centered in the northwestern North Pacific and hemispheric teleconnections. Kwon and Joyce (2013) showed that in this case the northward heat transport by the synoptic atmospheric eddies was decreased. In these studies, the meridional shifts of the KE were derived from temperature data at 200-m depth, with very limited spatial and temporal resolution. They were only moderately correlated (r=0.52) with the meridional shifts more accurately derived from satellite altimetry, probably because of the strong spatial smoothing and the relatively shallow level used to define the KE path. In addition, the temporal resolution was too coarse to investigate seasonal dependency in the air-sea coupling. More recently, O'Reilly and Czaja (2014) produced a more accurate KE index derived from a maximum covariance analysis between SST and SSH gradient observations, but SST observations with high spatial resolution were only available since June 2002, so that a longer KE index (1992-2011) was obtained by projecting the 2002-2011 SSH spatial pattern onto the full SSH record.

It is thus of interest to use data with higher temporal resolution that describe the KE variability over a longer duration, so that its influence on the atmosphere and its seasonal

143 dependency can be better assessed. In the present paper, we use the SSH-based KE index that
144 was derived by Qiu et al. (2014) by combining satellite SSH measurements and an eddy-
145 resolving ocean general circulation model (OGCM) hindcast, providing an accurate
146 description of the KE state at monthly resolution during the 1955-2012 period. Qiu et al.
147 (2014) showed that the KE fluctuations changed character around the 1976-77 regime shift in
148 the North Pacific climate system (Trenberth and Hurrell 1994). Here we focus on the 1979-
149 2012 period, which is characterized by large decadal fluctuations of the KE and is covered by
150 the ERA-Interim reanalysis (Dee et al. 2011). The data and method are described in section 2
151 and 3. In section 4, we show that the KE precedes a large-scale atmospheric signal in the cold
152 season, and we discuss the possible mechanisms by which the KE changes affect the large-
153 scale atmospheric circulation. In Section 5, the response asymmetry is analyzed. The results
154 are summarized and discussed in Section 6.
155

156 ## 2. Data

157 To represent the variability of the KE, we use the index of Qiu et al. (2014), which is
158 defined by the SSH anomaly averaged in the region (31°–36°N, 140°–165°E) (Fig. 1, cyan
159 curve). A positive KE index denotes a stable state in which the KE jet has a steady and
160 northerly path, an increased surface transport, an enhanced southern recirculation gyre, and a
161 decreased regional eddy kinetic energy. A negative KE index reflects the reversed properties.
162 From October 1992 to December 2012, the KE index is based on satellite altimeter
163 observations. To extend the time series prior to the satellite altimeter period, Qiu et al. (2014)
164 used a hindcast simulation of the eddy-resolving Ocean general circulation model For the
165 Earth Simulator (OFES) as it captures the KE decadal variability realistically (Nonaka et al.
166 2006; Taguchi et al. 2007; Qiu et al. 2014). The model output extends from 1950 to 2012, but
167 the KE index inferred from OFES exhibits shorter and less regular fluctuations prior to the

168 1976–77 North Pacific climate shift (Qiu et al. 2014). Here, we focus on the 1979-2012
169 period, which corresponds to the availability of the latest reanalysis of the European Centre
170 for Medium-Range Weather Forecasts (ECMWF) ERA-Interim (Dee et al. 2011). The mean
171 seasonal cycle of the KE index was subtracted by regression onto the first two annual
172 harmonics, which accounted for 2.4% of the total variance.

173 Monthly anomalies of sea level pressure (SLP), geopotential height, horizontal wind
174 velocity, wind stress, temperature and humidity were taken from ERA-Interim at 1.5°
175 resolution, while a ¾° resolution was used for SST, turbulent and radiative heat fluxes, and
176 vertical wind. Masunaga et al. (2015) have shown that the improvement of the resolution of
177 the prescribed SST in ERA-Interim (from 1° to ¼°) starting in January 2002 exerts substantial
178 impacts on the representation of the marine atmospheric boundary layer, cloudiness, and
179 precipitation. Hence, our analysis of the local influence of the KE variability should be
180 viewed with caution. Nonetheless, our results were verified using the NCEP-NCAR
181 reanalysis (Kalnay et al. 1996) that has a lower resolution (T63). This suggests that data
182 assimilation is sufficient to strongly constrain the large-scale atmospheric flow, and that the
183 improvement of the SST resolution in 2002 does not significantly influence our estimation of
184 the large-scale response to the KE fluctuations. Transient eddy activity and fluxes were
185 estimated from high-pass daily values, using the Blackmon filter to retain fluctuations with
186 periods between 2 and 8 days (Blackmon and Lau 1980; Hurrell and Deser 2009). In addition,
187 the latent and sensible heat fluxes were taken from the 1° OAFlux product (Objectively
188 Analysed air-sea Fluxes) provided by the Woods Hole Oceanographic Institution (Yu and
189 Weller 2007). Sea ice cover (SIC) and snow cover extent (SCE) datasets provided by NOAA
190 National Climatic Data Center (NCDC) were also considered. The SIC dataset comes from
191 the passive microwave monthly sea-ice concentration provided by the National Snow and Ice
192 Data Center. The SCE dataset is a record of weekly Northern Hemisphere snow cover extent

provided by the Rutgers University Global Snow Laboratory. As for the KE index, the mean seasonal cycle was removed from each variable.

3. Method for estimating the atmospheric response

To estimate the atmospheric response to the KE variability, we follow the lag regression approach of Frankignoul et al. (1998). Its principle is that, given the limited persistence of the atmosphere intrinsic variability compared to the oceanic one, ocean-to-atmosphere impact can be estimated by the covariance between the ocean and the atmosphere, with the ocean leading by more than the intrinsic atmospheric persistence but less than the oceanic one, which is about 2-3 years for the KE index. However, this requires that there be no other persistent signal in the atmosphere, which does not hold in the presence of trends and atmospheric teleconnections with the tropics. Hence, before calculating the regressions, a cubic polynomial estimated by least-squares fit was removed from each variable (linear detrending yields very similar results). The ENSO signal was also removed, as described in the appendix. The impact of this correction on the KE index is small, except during the strong ENSO events in 1982-83, 1997-98, 2003 and 2010 (Fig. 1).

To distinguish the atmospheric response to the KE variability from that to the OE front, we first used bivariate regression on the KE index and FSKA's index of the meridional shifts of the OE derived from the maximum meridional SST gradient, using the 1982-2012 period when both indices are available. As the results were very similar to those given by univariate regression, consistent with the poor correlation between the two indices ($r \sim 0.2$) (Fig. 1), only univariate regressions onto the KE index are shown below.

a. The statistical model

Earlier numerical modeling studies suggest that the atmospheric response to

anomalous SST or other boundary forcing in the extratropics takes 1-2 months to reach its maximum amplitude (Ferreira and Frankignoul, 2005; Deser et al. 2007). This delay reflects the time for eddy-mean flow interactions to transform the initial baroclinic local response into a large-scale equivalent barotropic one. However, recent high-resolution experiments suggest that the maximum amplitude may be reached slightly faster (Smirnov et al., 2015), so that we assume that the response time to the SST fingerprint of the KE is 1 month. As discussed in Frankignoul et al. (2011a), the monthly atmospheric fields have some persistence and a lag of 1 month may mix atmospheric forcing and response. Considering the ocean leading by at least 2 months is therefore the safest way to single out the response (see also section 4a). Moreover, the SST fingerprint of the KE becomes slightly stronger and more extended after a delay of 1 month (not shown), consistent with the prevalent role of SST advection in the KE region (Vivier et al. 2002). Hence, we assume that the atmospheric response time to the KE is 2 months, so that an atmospheric variable *X* is decomposed into:

$$X(t) = \alpha\, K(t-2) + b\, e(t-1) + n(t) \qquad (1)$$

where *K(t)* is the KE index, *e* is the ENSO signal and *n(t)* is the atmospheric noise, considered as white at low frequency. To take into account the time for ENSO teleconnections to reach the North Pacific, we have assumed a one-month delay, which corresponds to the maximum ENSO teleconnections, as estimated by the root mean square of the regression coefficients of North Pacific SLP (north of 20°N) onto the ENSO signal. To estimate α, we remove the ENSO signal, using the method of FSKA, which yields (Appendix 1)

$$\tilde{X}(t) = \alpha\, \tilde{K}(t-2) + n(t) \qquad (2)$$

where $\tilde{X}$ and $\tilde{K}$ denote the ENSO filtered atmospheric variable and KE index. As the KE index is standardized, the regression of $\tilde{X}(t)$ onto $\tilde{K}(t-2)$ provides an estimate of the typical amplitude of the response, corresponding to one standard deviation change in the KE index. In the following, such regressions are referred to as the estimated response to the KE variability (unless evidence is found that other concomitant boundary forcing may have contributed to the atmospheric response). Note that there is some arbitrariness in our choice, since the regressions when $\tilde{K}$ leads by 3 or 4 months show similar patterns (see Fig. 3 below). Estimating the response at lag 3 instead of lag 2 would slightly increase its amplitudes, as the covariance between $\tilde{X}$ and $\tilde{K}$ would be divided by the lag-1 autocorrelation of $\tilde{K}(t)$.

b. Statistical significance

Statistical significance was estimated in two ways, with comparable results. First we used a standard Student t-test in which the effective number of degrees of freedom N_{eff} is estimated as $N_{eff} = N\,\frac{1-r_1 r_2}{1+r_1 r_2}$ in order to take into account the time series persistence, where N is the sample size (132 in most cases, when we use 4 months for 33 years), and r_1 and r_2 are the lag-one autocorrelation of the KE index and the time series being regressed (Bretherton et al. 1999). Note that the KE index is highly persistent (r_1= 0.86 for the ASON season), but atmospheric time series have only little autocorrelation. The second method is a block bootstrap approach, randomly permuting the atmospheric time series 1000 times in blocks of 3 years (e.g. von Storch and Zwiers 1999). The Student t-test gives a slightly larger statistical significance. However, both approaches may well underestimate significance (Decremer et al. Tellus 2014). Hence, the student t-test is used in all figures except for vectors, whose significance was estimated by bootstrap scrambling.

4. Cold season atmospheric response to KE fluctuations

Consistent with the seasonal changes in the atmospheric dynamics, the ocean-atmosphere interactions exhibit strong seasonal variations (e.g., Czaja and Frankignoul 2002; Taguchi et al. 2012). Indeed, regressions on the KE index based on all months of the year largely differ from those only based on summer or winter months (not shown). Here, we focus on the cold season, when air-sea interactions are strongest in western boundary current regions because of large heat release to the atmosphere. A close examination of the cold season suggests that there also exist substantial month-to-month variations in the atmospheric response pattern. Figure 2 shows the regression of the geopotential height anomaly at 250hPa (hereafter Z250) on the KE index 2 months earlier in sliding sets of 2 months, from September-October (SO) to February-March (FM). A broadly coherent tripolar atmospheric response pattern is found from October to January, while it is not yet established in September-October, and becomes quite different in February-March. This is consistent with observational and modeling studies (Peng and Whitaker 1999; Liu and Wu 2004; Liu et al. 2007; Gan and Wu 2012; Taguchi et al. 2012) that show that the North Pacific Ocean feedback to the atmosphere is dominated by the early-winter response, and that the late winter one differs significantly. Note that ON and DJ show slightly different patterns, especially over the United States. The ON response is very similar to the one found by Okajima et al. (2014) for October 2011, while it is slightly different in DJ. Nonetheless, the analyses presented in this paper show broadly the same results if applied separately to the 2 periods (not shown). Hence, in order to maximize the number of degrees of freedom without substantially distorting the signal by seasonal changes, we focus on the atmospheric response estimated from monthly anomalies in October, November, December, and January (ONDJ). Note that we use monthly anomalies (four values per year at each grid point). However, using seasonal means gives very similar results.

a. Lead-lag analysis

One of the difficulties in estimating the midlatitude atmospheric response to oceanic fluctuations is to distinguish it from the atmospheric forcing that generated the oceanic variability. As discussed in Section 1, the low-frequency variability of the KE is largely controlled by large-scale wind stress curl variations that lead to oceanic adjustment via baroclinic Rossby wave propagation, which also initiates frontal-scale inertial fluctuations. The observations and linear Rossby wave models suggest that the KE is primarily forced by wind stress curl anomalies with a delay of 3-4 years (Ceballos et al. 2009; Qiu 2003). Hence, the covariance between the KE and the atmosphere leading by ~3-4 years shows the atmospheric forcing pattern. On the other hand, the covariance at lag ≥ 2 months (positive lag indicates that the KE leads) should reflect the atmospheric response to the KE if the ENSO signal is removed, and α can be estimated from (2). If there was no direct local forcing and the KE was only remotely forced, the covariance at lag ≤ 1 would also reflect the atmospheric response at short lag, as $\widetilde{K}(t)$ would be uncorrelated with prior values of *n(t)*. Hence, the lead-lag regression would be symmetric about lag 2, within sampling uncertainties. However, this is not the case as the KE also responds rapidly to the atmosphere, either because of local forcing or because of a fast barotropic adjustment, so that the covariance at lag ≤ 1 month mix atmospheric forcing and response.

The lead and lag relation between the KE index and SLP, Z250 and the Ekman pumping in ONDJ is illustrated by the regressions in Fig. 3. The atmospheric forcing of the KE is shown at lag -42, but a very similar pattern is found at lags -14 to -48, i.e. when the atmosphere leads the KE by 1.5 - 4 years. The atmospheric pattern broadly resembles the North Pacific Oscillation in its positive phase, with a negative Ekman pumping anomaly in the subtropical gyre and a positive one in the subpolar gyre. The regressions at lag ≥ 2 with

317 the ENSO signal removed reflect the atmospheric response to the KE. Because of the high
318 autocorrelation of the KE index (33-month zero crossing), the regression patterns are very
319 similar for lags between 2 and 6 months. On the other hand, the regression patterns at lag ≤ 1
320 are somewhat different, with a stronger SLP high in the Eastern Pacific. At lag ≤ 0, the ENSO
321 signal was not removed because it does not make sense to remove ENSO when looking at the
322 atmospheric forcing of the KE variability, since the KE responds as an integrator of the
323 forcing, which includes the ENSO teleconnections. However, the differences between lead
324 and lag are even larger when ENSO is removed (not shown), confirming that lag ≤ 1 mix
325 atmospheric forcing and response.
326 The ONDJ atmospheric response is thus best detected when the KE leads by at least 2
327 months. The following analysis is mostly based on lag 2, shown again for clarity in Fig. 4.
328 The atmospheric response in ONDJ consists of a high over the central and Northwest Pacific,
329 typically reaching 0.6 hPa at sea level and 20 m at 250 hPa, and a low of similar amplitude
330 over Alaska and Canada. There is also a smaller high over western United States at 250 hPa.
331 The structure appears to be broadly barotropic with a westward tilt with height, characteristic
332 of baroclinicity. The associated zonal-mean zonal wind anomaly (not shown) has a deep
333 vertical structure up to 50 hPa that is statistically significant, with positive anomaly of 1 to 2
334 m/s at ~55°N and negative anomaly of 2 to 3 m/s at ~35°N, indicating a poleward shift of the
335 eddy driven jet. This suggests that the atmospheric response to the KE decadal fluctuations is
336 closely associated with changes in the transient eddy activity. The Ekman pumping anomaly
337 is positive south of 35°N, and negative to the north of it, opposite to the atmospheric forcing
338 pattern (at lag=-42), albeit slightly shifted to the south. This suggests a negative feedback on
339 the KE changes, in agreement with Qiu et al. (2014, their Fig. 6), who found a broadly similar
340 but less noisy pattern by considering all the months of the year. The following analysis
341 attempts to explain the mechanisms by which the KE variability leads to such atmospheric

342 response.

343 It should be noted that the atmospheric response seems to be primarily driven by the
344 decadal variability of the KE. Indeed, repeating the analysis, but regressing onto a high and a
345 low pass-filtered KE index with a cut-off at 6 years gave very similar results when using the
346 low-pass filtered KE index, but different and more noisy ones when using the high-pass
347 filtered one (not shown).

348

349 b. SST anomalies and heat flux feedback

350 The KE variability influences the atmosphere through SST changes that generate air-
351 sea heat flux anomalies (Fig. 5). For an atmospheric response time of 1 month, the SST in
352 SOND should be considered. It shows a broad warming of typically ~0.3 to 0.5 K in the KOE
353 region, which is in part driven by the intensified advection of warm water coming from the
354 subtropics, as discussed by Vivier et al. (2002), Kelly et al. (2010), and Qiu et al. (2014),
355 among others. The warming is much broader than that associated with the meridional shifts of
356 the KE front east of 155°E during winter (Seo et al. 2014), presumably because the index of
357 Qiu et al. (2014) represents more general KE changes, including the eddy activity that
358 strongly affects the SST and might spread the warming. The surface easterlies response to the
359 KE may also provide a positive feedback as anomalous Ekman transport brings warm water
360 into the KOE region. Although the SST pattern may be artificially broad due to the low
361 resolution of ERA-Interim, recent studies have shown that the KE generates a northeastward
362 quasi-stationary driven jet that separates from the KE around 155°E and transports subtropical
363 water to the subarctic region (Isoguchi et al. 2006; Sugimoto 2014; Wagawa et al. 2014). The
364 KE can therefore have an influence on the SST much further north than its mean path, and in
365 particular along the OE front, as seen in Fig. 5a, where the SST anomaly is maximum north of
366 the KE mean path, in the confluence region, just south of the OE front. This suggests that,

even if the KE and OE indices are not strongly correlated (Fig. 1), there might be some influence of the KE on the OE front that does not significantly impact its latitude.

There is no warming in the western end of the confluence zone where the SST is strongly affected by warm eddies (Sugimoto and Hanawa 2011). These eddies are fewer when the KE index is positive, especially west of 150°E, thus possibly opposing the intensified advection. There are also small remote SST anomalies that co-vary with the KE. They may reflect the SST response to atmospheric changes forced by the KE or SST variations forced by the atmospheric fluctuations that affect the KE on short time scale, since they disappear for lags larger than a few months (not shown). In particular, the cooling in the subpolar gyre could be attributed to the intensification of the westerly winds coming from northeastern Siberia due to the high pressure anomaly that precede the KE (Fig. 3), generating anomalous southward Ekman transport. The meridional SST gradient anomaly is positive on the northern flank of the OE east of 150°E, and negative to the south of it (Fig. 5b). Since the climatological SST gradient is maximum along the OE, the OE front is more extended eastward and slightly shifted north when the KE is in positive phase, as remarked above. Note that the concomitant SST anomalies in the other ocean basins are small.

Frankignoul et al. (1998) have shown that the thermal forcing generated by SST anomalies can only be determined when the heat flux lags SST by at least one month. It is indeed after a lag of 2-3 months that the heat flux feedback is observed. The anomalous net surface heat flux (latent + sensible + longwave + shortwave) at lag 2 is dominated by the turbulent heat flux, and tends to be positive (heat loss from the ocean) in the KOE region, suggesting a damping of SST anomalies, i.e. a negative feedback (Fig. 5c). This does not hold immediately off Japan where the SST anomalies are negligible, presumably because the turbulent heat flux in the Kuroshio-Oyashio Confluence Region strongly responds to anticyclonic (warm) eddies, which are less active when the KE index is positive (Sugimoto

and Hanawa 2011). However, the heat flux pattern is noisy, and OAFlux may not fully resolve the influence of the KE variability because its estimation relies on atmospheric reanalysis data with relatively low horizontal resolution. Interestingly, the heat flux feedback is clearer one month later, in NDJF, as shown in Fig. 5d where the heat flux lags the KE index by 3 months. This does not reflect the larger time lag, but atmospheric seasonal differences as the heat flux feedback is stronger during winter (Frankignoul and Kestenare 2005; Park et al. 2005). This could also be due to the interannual to decadal variability of the East Asian monsoon and the associated air-sea heat exchange over the KOE region in early winter (Nakamura and Yamagata 1999; Nakamura et al. 2002; Yoshiike and Kawamura 2009; Kwon et al. 2010). Very similar results are found with the turbulent heat flux from ERA-Interim instead of OAFlux, but it also suffers from limited resolution (section 2).

c. Changes in convection and synoptic activity

In order to explore the dynamical mechanisms involved in the ocean-to-atmosphere interaction, we show the estimated response in ONDJ of several key atmospheric variables, which are thus in phase with the atmospheric response in Fig. 4. The warming of the KOE region generates a positive air temperature anomaly that extends throughout the troposphere and tilts northward with height, with maximum amplitude of 0.6 K at the 400 hPa level (Fig. 6a). There is a significant anomalous upward motion in the longitude-band of 155°–175°E, on the northern side of the KE, where the SST anomaly is maximum. Albeit not statistically significant, there is downward motion north and south of it, like in the simulated response to an OE shift in Smirnov et al. (2015). The upward motion is strongest at 850 hPa, near the top of the marine atmospheric boundary layer, and it reaches 400 hPa, with a northward tilt with height, as above the Gulf Stream (Minobe et al. 2010). The positive SST anomaly thus contributes to the destabilization of the air column above it, and the convective available

potential energy is indeed increased (not shown). Although very noisy, there is a positive anomaly in convective precipitation over the KOE region, which leads to a small but significant correlation of about 0.17 when lagging the KE index by 1 to 12 months if it is averaged over the KOE warming (not shown). Although no net precipitation anomaly could be found, possibly because ERA-Interim precipitation is questionable due to very few observations and pronounced spin-up effects over oceans and midlatitude storm tracks (Dee et al. 2011), we conclude that convection is enhanced. This suggests wind convergence at low level, but no corresponding response in the surface wind stress was found.

The KE variability has a strong impact on the synoptic-scale activity, as shown by the Eady growth rate anomaly at 850 hPa (Fig. 7a). The Eady growth rate is given by $\sigma = 0.31 \frac{|f| \left|\frac{\partial V(z)}{\partial z}\right|}{N}$, where f is the Coriolis parameter, V(z) the vertical profile of the horizontal wind, and N the Brunt Väisälä frequency. It measures the theoretical growth rate of the most unstable synoptic mode, and it was verified that it is largely determined by the air temperature gradient, because of the thermal wind balance. A strong negative anomaly appears on the southern flank of the KE due to the weaker SST gradient (Fig. 5b), while the opposite occurs over western Canada. Given the location of the climatological Eady growth rate maximum (green curve), the anomaly pattern indicates a weakening along the KE and a slight downstream northeastward extension of the zone of maximum baroclinicity. Downstream of the Eady growth rate anomaly, the storm track is increased over the eastern North Pacific and Alaska, as shown in Fig. 7b by the anomaly in the root-mean-square of 500 hPa geopotential height. Chang (1993) has shown that the downstream development of unstable baroclinic waves is the main mechanism by which the storm track is extended from highly unstable regions (western North Pacific) into relatively stable regions downstream (eastern North Pacific). Such downstream impact on storm track is also in agreement with Rivière (2009), who showed that latitudinal variations of the Eady growth rate generate a positive eddy

feedback that amplifies the variations downstream of the source region. They also showed that a more poleward baroclinicity favors anticyclonic wave breaking (AWB) events. This pushes the eddy driven jet poleward, favoring AWB in the region of maximum eddy activity and leading to a more SW-NE orientation of the jet. This should lead to an anticyclonic anomaly in the central basin and is in agreement with the northward shift of zonal wind discussed above and with the SLP response in Fig. 4. Hence, by means of baroclinic waves and eddy activity, the impact on the storm track of the KE warming is primarily downstream.

To document the KE influence on the meridional heat and moisture transfer by the transient eddies, the transient eddy heat and moisture fluxes, <v'T'> and <v'q'>, respectively, were considered, where the prime denotes high-pass daily values and < > monthly averages. The anomalies driven by the KE fluctuations are given at the 850 hPa level in Fig. 7c,d, but very similar results are found for the integrated transports between 950 hPa and 700 hPa. For both fluxes, there is a positive anomaly in the eastern North Pacific, on the northeastern flank of the climatological maximum, and a negative anomaly on the southern flank. This indicates a weakening and a northeastward extension of the zone of maximum transient eddy fluxes, consistent with the changes in Eady growth rate and storm track. This is slightly different from the northward shift found by Qiu et al. (2014) using all the months of the year. In zonal averages, the meridional eddy humidity transport is weakened during a positive KE phase, in agreement with Kwon and Joyce (2013), although they found a very different spatial pattern using the KE index based on the temperature at 200 m depth in JFM. On the other hand, the zonally-averaged eddy heat transport is weakened at ~35°N but enhanced at ~60°N because of the large positive anomaly over Alaska.

d. An influence up to the stratosphere

The SST-driven changes in atmospheric stability and transient eddy activity are likely

467 the main mechanisms by which the KE has an influence in the upper atmosphere. The vertical
468 profile of the geopotential height anomaly shows a maximum at the 250 hPa level, above the
469 maximum temperature anomaly (the maximum geopotential height and temperature
470 anomalies occur where the corresponding mean vertical gradient is maximum), and a strong
471 anomaly in the stratosphere (Fig. 6). The hemispheric Z250 teleconnection pattern (Fig. 8a)
472 reveals a low over the Chukchi Sea and a high over United States.

473 In order to understand how the signal propagates into the whole hemisphere, we show
474 the anomalous Wave Activity Flux (WAF) at 250 hPa (the same is found at 500 hPa) derived
475 from the monthly geopotential height and temperature anomalies, following the formulation
476 of Takaya and Nakamura (2001), which is a generalization of Plumb's (1985) flux applicable
477 to a zonally-varying basic flow. The WAF is a diagnostic tool for illustrating the propagation
478 of quasi-geostrophic stationary Rossby waves. Its divergence (convergence) gives the source
479 (sink) of wave activity, and it is, in principle, independent of wave phase and parallel to their
480 local three-dimensional group velocity. It is therefore suited for a snapshot diagnostic of wave
481 packets of stationary eddies, but it is not a momentum flux, unlike the Eliassen-Palm flux. Fig.
482 8a shows that the KOE region is a source of wave activity propagating primarily poleward
483 toward the low over the Chukchi Sea. There is also some hint of a wavy propagation toward
484 the high anomaly over western United States. This wavy propagation from the KOE region to
485 United States going through the Artic is even clearer in the lower stratosphere, at 100 hPa
486 level (Fig. 8b). Hence, this analysis suggests that stationary Rossby waves play an important
487 role in extending the atmospheric response poleward and eastward.

488 Interestingly, one month later, in NDJF, the low-pressure lobe is elongated over
489 Greenland and the North Atlantic, reflecting a strengthened polar vortex, the high-pressure
490 lobe over western United States has spread eastward, and a significant anomalous high is
491 found over northwestern Europe (Fig. 8c,d). The pattern has some similarity with the Arctic

Oscillation, albeit slightly shifted poleward, displacing the eddy-driven jet northward. The wave activity flux may explain the spreading over the Arctic and United States, but it shows no significant link to western Europe. As there is little change in the SST anomalies in NDJF and no significant SST anomalies are observed in the North Atlantic (not shown), the spreading toward Europe cannot be attributed to downstream or remote changes in SST. Therefore, the anomalous high over Europe might come from a downward propagation of the stratospheric vortex changes into the troposphere, thus influencing the North Atlantic Oscillation (Baldwin and Dunkerton 1999; Polvani and Waugh 2004). Alternatively, the high over northwestern Europe could be due to the KE-driven changes in the storm track. Indeed, the North Atlantic storm track activity depends in large part on the Pacific storm track behavior via the link between synoptic wave breaking events in the eastern Pacific and the Atlantic (Chang 2004; Drouard at al. 2013). Disturbances in the Pacific could therefore induce changes in the Atlantic. In fact, the storm track in NDJF is strengthened over northwestern Canada and Iceland (not shown), which could trigger the anomalous high over Europe through eddy-mean flow interactions. However, the E-vector divergence anomaly (Hoskins et al. 1983) was too noisy to confirm this hypothesis. Another possible explanation could be that the Pacific-induced anomaly is trapped and redistributed by the time-mean tropospheric jets, which act as waveguides (Branstator 2002).

Although stationary Rossby waves play an important role in spreading the signal horizontally, the strengthening of the polar vortex implies that the upward injection of planetary-wave activity from the troposphere to the stratosphere is reduced (Baldwin et al. 1999; Polvani and Waugh 2004). To confirm this hypothesis, we consider the zonally averaged meridional eddy heat flux [v*T*] at 100 hPa, where the asterisks denote departures from the zonal mean, which is a diagnostic of the troposphere-to-stratosphere wave activity propagation (Polvani and Waugh 2004), and is directly proportional to the vertical component

517 of the conventional Eliassen-Palm flux (Andrews et al. 1987; Nishii et al. 2010). As shown in
518 Fig. 9b, the positive phase of the KE is followed by a reduced wave activity entering the
519 stratosphere, and the spatial distribution of v*T* (Fig. 9a) indicates that the reduced wave
520 activity primarily takes place north of the KOE. The same result is obtained when using the
521 vertical WAF from Takaya and Nakamura, but with less statistical significance (not shown).
522 In summary, anomalous wave activity flux propagates horizontally from the KOE region and
523 contributes to spreading the signal poleward and eastward (Fig. 8a,b), but less wave activity
524 flux penetrates into the stratosphere, strengthening the polar vortex one month later (Fig. 8d).
525

526 **e. Impact on near-surface climate**

527 The atmospheric response to KE fluctuations has significant impacts on near-surface
528 climate. As expected from the SST signature of the KE variability, the air temperature in the
529 KOE region is warmer (Fig. 10a). There is also a significant warming over western and
530 central North America, northeastern Asia, and northern Africa. This warming is likely the
531 cause of the concomitant reduced snow cover extent seen in Fig. 10b, since it only appears
532 when the KE index leads by at least 2 months. Consistent with the anomalous low, the
533 temperature over the Arctic Ocean is colder. However, although significant, the temperature
534 perturbations are small, and the potential predictability over these regions based on the KE
535 index is overall limited. This was investigated conducting a one year out-cross validation. For
536 each year and grid point, we perform the lag regression of the air temperature on the KE index
537 while removing this year, and we use the regression to predict the removed year. The
538 predicted air temperature time series is then correlated to the observed one. This analysis
539 suggests statistically significant, albeit limited, potential predictability over the KOE region
540 and the northern central and western United States, where the cross-validated correlation only
541 reaches 0.2 (0.3 for seasonal means). Later in winter, the weak warming over Iceland is

542 reinforced and has propagated toward northern Europe (not shown). Cross-validation suggests
543 that at 3 and 4 months lead there is a weak potential predictability over the United States and
544 northwestern Europe.
545

546 # 5. Asymmetry

547 To investigate whether the stable and the unstable states of the KE influence the
548 atmosphere in a symmetric way, composites were constructed for the response to large
549 positive and negative KE events, namely when the absolute value of the KE index for
550 individual months of the ASON season is higher than one standard deviation. As indicated by
551 the red and blue dots in Fig. 1, the sample is limited, as 27 months qualify as positive events
552 and 24 months as negative events. Therefore, the results should be considered with caution,
553 although asymmetric regression analysis gives basically the same results (not shown). Also,
554 the same analysis was conducted for seasonal means, and the results are identical.
555 A significant asymmetry is found in the large-scale atmospheric response, but much
556 less in the local features. The SST anomaly in the KOE region is roughly symmetric in pattern
557 and amplitude, although the negative anomaly is more longitudinally extended (Fig. 11a,b).
558 There are also clear effects of the oceanic eddy activity. During the positive state, eddy
559 activity is much weaker, in particular west of 150°E. The warming is therefore only observed
560 east of 150°E, whereas the cooling during the negative phase is found much closer to the
561 Japanese coast. Also, the anomalies on either sides of the KOE region are asymmetric. A
562 negative SST anomaly is found in the subtropical gyre when the KE is in a stable state, while
563 a positive SST anomaly in the subpolar gyre is found in the unstable state. Hence, as shown
564 by the meridional SST gradient in Fig. 12, a positive event is associated with a stronger and
565 northward-shifted SST front near the OE, while negative events are linked to a weaker and
566 southward-shifted SST front. The heat flux anomaly is broadly symmetric, more clearly so in

NDJF, primarily reflecting the heat flux feedback (not shown). Stronger differences are seen in the Eady growth rate anomaly, as there is a strong weakening of the baroclinicity along the KE during the positive phase, so that the region of maximum baroclinicity is weakened, while it is only slightly shifted south during the negative phase (Fig. 11c,d). Since the baroclinicity is largely determined by the temperature gradient, this is consistent with the strong asymmetry in the air temperature anomaly discussed below. The storm track is enhanced in the northeastern Pacific during a positive phase, while there is no clear signal during a negative phase, but only small patches of positive anomaly all around the climatological maximum (Fig. 11e,f). This suggests that the storm track is less anchored in this case, which might result from the weaker SST front along the OE (Fig. 12), consistent with the anchoring mechanism of Nakamura et al. (2004).

The large-scale atmospheric response reveals an even stronger asymmetry. During the stable KE state, the SLP and Z250 anomalies reflect the regression analysis above, except that the North Pacific high is broader and more extended eastward than in Fig. 4 (Fig. 13a,b). The WAF indicates propagation in both the north and the south direction, which may explain the weak low-pressure anomaly in the subtropics. However, the propagation does not reach the tropics as far as in Miyasaka et al. (2014), since it does not spread further south than 16°N. During the unstable KE state, on the other hand, the atmospheric response is small and noisy. It is reduced to a more localized high over the KOE region and a downstream low which are 3 times weaker than the anomalous high during the stable state, and also tilt westward with height (Fig. 13c,d). The WAF indicates that this region is a source of eastward stationary Rossby wave propagation, but not of poleward one, so it is not clear that the positive anomaly over Canada and western United States is linked to the KE.

The asymmetry can be attributed to the fact that, although the SST anomalies are similar in amplitude, a positive SST anomaly has a stronger impact on the air column above it

than a negative SST anomaly. As discussed in Deser et al. (2004), such asymmetry is due, in small part, to the non-linear dependence of evaporation upon SST according to the Clausius-Clapeyron relation, and in larger part by the differences in the deep convective component of the anomalous heating. Indeed, cooling from below is an inherently stabilizing process while heating from below is a destabilizing one, conducive to convective overturning and deeper vertical penetration. Similarly, Sheldon and Czaja (2014) have shown that during winter, convective instabilities are very frequent over the KOE region, and a lower SST would lead to fewer occurrences, while a warmer SST would increase it. As shown in Fig. 14, although the temperature anomaly within the boundary layer has similar amplitude for positive and negative phases of the KE, the positive anomaly amplifies with height, while the negative one does not, so the temperature anomaly in the mid-troposphere is considerably stronger in the positive case, consistent with the geopotential anomaly. As a stronger temperature anomaly has a stronger impact on baroclinicity, the changes in baroclinicity and storm track are small in the negative case compared to the positive one (Fig. 11c-f). Since baroclinicity and storm track anomalies are likely the mechanisms by which a local response leads to a large-scale atmospheric signal, the atmospheric response in the unstable state remains localized, and teleconnections are almost non-existent.

6. Summary and conclusions

Using the KE index of Qiu et al. (2014), we have shown by regression and composite analyses that the decadal variability of the KE has a significant influence on the large-scale atmospheric circulation in the northern hemisphere during the cold season. A close examination of the month-to-month variability in the atmospheric response pattern led to the focus on the months between October and January (ONDJ), when the atmospheric response is

617 broadly coherent. This is consistent with the observational and modeling studies (Peng and
618 Whitaker 1999; Liu et al. 2007; Gan and Wu 2012; Taguchi et al. 2012) that showed that the
619 North Pacific SST feedback to the atmosphere is dominated by the early-winter atmospheric
620 response, and that the response differs in late winter.

621 When the KE is in stable state (positive KE index), during which the KE jet is
622 strengthened, shifted northward, and the regional eddy kinetic energy is lower, enhanced
623 advection by the mean flow generates a broad positive SST anomaly of typically ~0.4 to 0.6
624 K in the KOE region, leading to a stronger and more eastward extended OE front, possibly
625 via the eddy driven jet described in Wagawa et al. (2014), although it does not substantially
626 impact the OE latitude. This warming enhances the heat release to the atmosphere (negative
627 heat flux feedback), in agreement with Qiu et al. (2014) and Joyce et al. (2009). The heat flux
628 anomaly leads to a significant upward motion above the SST anomaly maximum and an
629 increase in the convective available potential energy and convective precipitation above the
630 warm SST. However, no corresponding anomaly in the surface wind convergence or the net
631 precipitation was found. Baroclinicity is weakened along the KE, and there is a northeastward
632 downstream extension of the eddy heat and humidity fluxes and the storm track. This is
633 consistent with Rivière (2009) who showed that latitudinal variations in the Eady growth rate
634 generates positive eddy feedback that amplifies the variation downstream of the source region.
635 The impact on eddy activity and storm track is probably the mechanism that generates
636 stationary Rossby waves that propagate from the KOE region toward the Arctic and western
637 United States. The hemispheric response thus consists of a high in the central and western
638 North Pacific, and a low over Alaska and the Chukchi Sea, and a weaker high over western
639 United States. There is a westward tilt with height, characteristic of baroclinicity. The
640 amplitude of the signal is limited, however, typically reaching 0.6 hPa at sea level and 20 m at
641 250 hPa. This is broadly comparable to the amplitude of the response to a shift of the Oyashio

642 Extension found by FSKA and in the modeling study of Smirnov et al. (2015), where the
643 response difference between the warm and cold high-resolution experiments is about 3 hPa at
644 sea level and 50 m at 300 hPa for a SST difference along the Oyashio Extension of 2 to 3 K.
645 The disturbance in the upper troposphere leads to reduced injection of wave activity in
646 the stratosphere, strengthening the polar vortex one month later, in NDJF, when the
647 atmospheric response is extended towards Europe and has some similarity with a positive
648 phase of the Arctic Oscillation. The wave activity explains the signal over the Arctic and
649 United States, but the signal over Europe is more likely due to downward propagation of the
650 stratospheric polar vortex changes into the troposphere (Baldwin and Dunkerton 1999;
651 Polvani and Waugh 2004) or to changes in the storm track and eddy-mean flow interactions
652 (Chang 2004; Drouard et al 2013). These teleconnections have a small but significant climatic
653 impact, albeit with very limited potential predictability, with cooling in the Arctic and heating
654 over Asia and United States, where the snow cover extent is reduced.
655 Composite analysis suggests a significant asymmetry in the large-scale atmospheric
656 response. While a strong impact on the large-scale atmospheric circulation is found during the
657 KOE warming (positive phase), there is little large-scale response during the negative phase.
658 This asymmetry may result from the difference between positive and negative SST impact on
659 the overlying atmosphere, as a positive temperature anomaly leads to more convective
660 instabilities and deeper vertical penetration in the atmosphere (Deser et al., 2004; Sheldon and
661 Czaja, 2014). Indeed, the air temperature anomaly has a deep vertical structure and amplifies
662 with height in the positive case, but not in the negative case. The positive KE phase has
663 therefore a strong impact on baroclinicity and transient eddies, which produce a large-scale
664 atmospheric response, while the negative phase only has a local impact.
665 While our results are in agreement with the study of Qiu et al. (2014), who used the
666 same KE index but did not distinguish between seasons nor explore the tropospheric response,

667 they differ from other studies based on estimated meridional shifts of the KE. This is perhaps
668 because Qiu et al.'s (2014) index does not simply reflect a latitudinal shift of the KE front, but
669 a much broader dynamical state oscillation, which leads to a different SST signature and thus
670 a different impact on the atmosphere. It might also be because different periods were
671 considered. FSKA found an equivalent barotropic high centered in the northwestern North
672 Pacific and a much weaker low over the KOE region in response to a northward shift of the
673 KE during 1980-2006, using a KE index with very limited spatial and temporal resolution, so
674 that no distinction was made between seasons. In addition, it was based on temperature
675 profiles that may be too shallow to accurately define the KE path. O'Reilly and Czaja (2014)
676 found that, during the 1992-2010 period, the transient eddy heat transport in winter and spring
677 has a dipolar structure with an increase in the west North Pacific and a decrease in the east
678 when the KE is shifted north and the SST front is stronger, unlike in the present analysis.
679 They used (unlagged) composites based on an index derived from a maximum covariance
680 analysis between SST and SSH gradients during 2002-2010. In this period, their index is very
681 similar to Qiu et al.'s (2014) index, and we verified that the two indices lead to similar
682 regression patterns in SLP, geopotential, Eady growth rate and eddy heat transport, albeit
683 different from those discussed here, presumably because the sample is too short to emphasize
684 the decadal KE changes that dominate the response in the present paper. However, the KE
685 indices differ considerably during 1992-2001 when O'Reilly and Czaja's index was extended
686 by SSH projection, with much larger decadal changes in Qiu et al.'s (2014) index. Whether
687 the differences in the two analyses are primarily due the differences in the KE indices or their
688 dominant time scale, or non-stationarity in the atmosphere, remains to be established.
689 On the other hand, our results are broadly comparable with the observational and
690 modeling studies of Liu et al. (2007) and Gan and Wu (2012) who considered the averaged
691 SST anomaly over the KOE region. In early winter (NDJ), they found a warm SST-equivalent

barotropic high response over the central North Pacific, and a low over Alaska and western United States. Similarly, our results do not substantially differ from those obtained with the method used by Taguchi et al. (2012) - a regression onto the SST in a box of 5° latitude centered on the OE - when it is applied to the 1979-2012 period considered here (not shown). However, Taguchi et al. found that in the 1956-2006 period the atmospheric response to their OE SST index in early winter consisted of a weakening of the Aleutian low, which differs from the central and Northwest Pacific high found in this paper. This again suggests that there may be changes in the atmospheric response over time, presumably linked to changes in the large-scale atmospheric circulation and the transient eddy feedback, which play a critical role in the atmospheric response (Peng and Whitaker 1999). Also, the relation between the KE and OE influence on the atmosphere needs to be investigated further.

Appendix 1. Removing ENSO teleconnections

Some care is required to estimate the atmospheric response to extratropical boundary forcing in the presence of ENSO teleconnections. To remove the ENSO signal from atmospheric variable *X(t)*, we define

$$\tilde{X}(t) = X(t) - Ae(t-1) \quad \text{(A1)}$$

where $A = \frac{C_{Xe}(1)}{C_{ee}(0)}$ is the regression of *X(t)* on *e(t-1)* and $C_{xy}(\tau)$ denotes the covariance between *x* and *y* at lag τ. Replacing in (1) yields

$$\tilde{X}(t) = \alpha K(t-2) + (b - \frac{C_{Xe}(1)}{C_{ee}(0)})\, e(t-1) + n(t) \quad \text{(A2)}$$

Estimating α by regression of $\tilde{X}(t)$ on $K(t-2)$, as often done, does not entirely remove the ENSO effects. To get an unbiased estimate, we define a modified KE index

$$\tilde{K}(t) = K(t) - Be(t+1) \quad \text{(A3)}$$

where $B = \frac{C_{Ke}(-1)}{C_{ee}(0)}$ is the regression of *K(t)* on *e(t+1)*. Replacing in (A2) yields

$$\tilde{X}(t) = \alpha \tilde{K}(t-2) + (b + \alpha \frac{C_{Ke}(-1)}{C_{ee}(0)} - \frac{C_{Xe}(1)}{C_{ee}(0)}) e(t-1) + n(t) \quad \text{(A4)}$$

Since *n* and *e* are uncorrelated, one has from (1)

$$C_{Xe}(1) = \alpha C_{Ke}(-1) + b C_{ee}(0) \quad \text{(A5)}$$

so that (A4) reduces to Eq. (2).

The reasoning is easily generalized to several ENSO indices. Here the ENSO signal is defined by the first two principal components (R-PCs), after rotation of the EOFs, of monthly SST anomalies in the tropical Pacific between 12.5°N and 12.5°S. To take into account the asymmetry and the seasonality of the ENSO teleconnections, the regression is done separately for positive and negative values of the R-PCs, and the regression coefficients are seasonally varying, with the multivariate regression for a particular calendar month also using the preceding and the following month. The ENSO removal for a particular month, say February, is thus based on regressions from January through March (JFM) on the two ENSO R-PCs one month earlier (in DJF) estimated separately for positive and negative values of the R-PCs:

$$\tilde{X}(feb) = X'(feb) - \sum_{i=1}^{2} \alpha_i^+ (JFM) * PC_i^+(jan) - \sum_{i=1}^{2} \alpha_i^- (JFM) * PC_i^-(jan) \quad \text{(A6)}$$

with

$$\alpha_i^{\pm}(JFM) = \frac{\sum X^{\pm\prime}(JFM) * PC_i^{\pm\prime}(DJF)}{\sum PC_i^{\pm\prime}(DJF) * PC_i^{\pm\prime}(DJF)}$$

where the + (–) index indicates positive (negative) values of the R-PCs, and the prime departure from the mean. Only very small SST anomalies were associated to the KE

738 fluctuations in the other tropical oceans, and the results are similar when calculating the EOFs
739 in the Indo-Pacific tropical region.
740
741
742 *Acknowledgements.*
743 This research has received funding from the European Union 7th Framework Program (FP7
744 2007-2013) under grant agreement n.308299 (NACLIM), from NSF grant AGS CLD
745 1035423, and from Agence Nationale de la Recherche under the reference ANR 2011 Blanc
746 SIMI 5-6 014 01. We thank Takafumi Miyasaka and Hisashi Nakamura for providing the
747 wave-activity flux code, Chris O'Reilly for providing his KE index, and Bunmei Taguchi and
748 Francis Codron for stimulating discussion. We also thank the reviewers for their constructive
749 and helpful comments on a previous version of this paper.
750
751
752 *References*
753 Andrews, D. G., J. R. Holton and C. B. Leovy, 1987: *Middle Atmosphere Dynamics*.
754 Academic Press, 489 pp.

755 Baldwin, M.P. and T. J. Dunkerton, 1999: Propagation of the Arctic oscillation from the
756 stratosphere to the troposphere. *J. Geophys. Res.*, **104**(D24), 30,937-30,946.

757 Bengtsson, L., K. I. Hodges, and E. Roeckner, 2006: Storm tracks and climate change. *J.*
758 *Climate*, **19**, 3518–3543.

759 Blackmon, M. L., and N.-C. Lau, 1980: Regional characteristics of the northern hemisphere
760 wintertime circulation: A comparison of the simulation of a GFDL general circulation
761 model with observations. *J. Atmos. Sci.*, **37**, 497–514.

762 Branstator, G., 2002: Circumglobal teleconnections, the jet stream waveguide, and the North
763 Atlantic oscillation. *J. Climate*, **15**, 1893–1910.

764 Bretherton, C. S., M. Widmann, V. P. Dymnikov, J. M. Wallace, and I. Bladé, 1999: The
765 effective number of spatial degrees of freedom of a time-varying field. *J. Climate*, **12**,
766 1990–2009.

767 Ceballos, L. I., E. Di Lorenzo, C. D. Hoyos, N. Schneider, and B. Taguchi, 2009: North
768 Pacific gyre oscillation synchronizes climate fluctuations in the eastern and western
769 boundary systems*. *J. Climate*, **22**, 5163–5174.

770 Chang, E. K. M., 1993: Downstream development of baroclinic waves as inferred from
771 regression analysis. *J. Atmos. Sci.*, **50**, 2038–2053.

772 ——, 2004: Are the northern hemisphere winter storm tracks significantly correlated? *J.*
773 *Climate*, **17**, 4230–4244.

774 Czaja, A., and C. Frankignoul, 2002: Observed impact of Atlantic SST anomalies on the
775 North Atlantic Oscillation. *J. Climate*, **15**, 606–623.

776 Decremer, D., C. E. Chung, A. M. L. Ekman, and J. Brandefelt, 2014: Which significance test
777 performs the best in climate simulations? *Tellus A*, **66**, 23139, 2014.

778 Dee, D. P., and Coauthors, 2011: The ERA-Interim reanalysis: configuration and performance
779 of the data assimilation system. *Quart. J. Roy. Meteor. Soc.*, **137**, 553–597.

780 Deser, C., G. Magnusdottir, R. Saravanan, and A. Phillips, 2004: The effects of North
781 Atlantic SST and sea ice anomalies on the winter circulation in CCM3. Part II: Direct
782 and indirect components of the response. *J. Climate*, **17**, 877–889.

783 ——, R. A. Tomas, and S. Peng, 2007: The transient atmospheric circulation response to
784 North Atlantic SST and sea ice anomalies. *J. Climate*, **20**, 4751–4767.

785 Drouard, M., G. Rivière, and P. Arbogast, 2013: The North Atlantic oscillation response to
786 large-scale atmospheric anomalies in the northeastern Pacific. *J. Atmos. Sci.*, **70**,
787 2854–2874.

788 Ferreira, D., and C. Frankignoul, 2005: The transient atmospheric response to midlatitude
789 SST anomalies. *J. Climate*, **18**, 1049–1067.

790 Frankignoul, C., and E. Kestenare, 2005: Air–sea interactions in the tropical Atlantic: A view
791 based on lagged rotated maximum covariance analysis. *J. Climate*, **18**, 3874–3890.

792 ——, and N. Sennéchael, 2007: Observed influence of North Pacific SST anomalies on the
793 atmospheric circulation. *J. Climate*, **20**, 592–606.

794 ——, A. Czaja, and B. L'Heveder, 1998: Air-sea feedback in the North Atlantic and surface
795 boundary conditions for ocean models. *J. Climate*, **11**, 2310–2324.

796 ——, N. Chouaib, and Z. Liu, 2011a: Estimating the observed atmospheric response to SST
797 anomalies: maximum covariance analysis, generalized equilibrium feedback
798 assessment, and maximum response estimation. *J. Climate*, **24**, 2523–2539.

799 ——, N. Sennéchael, Y.-O. Kwon, and M. A. Alexander, 2011b: Influence of the meridional
800 shifts of the Kuroshio and the Oyashio extensions on the atmospheric circulation. *J.*
801 *Climate*, **24**, 762–777.

802 Gan B. and L. Wu, 2012: Modulation of atmospheric response to North Pacific SST
803 anomalies under global warming: A statistical assessment. *J. Climate*, **25**, 6554–6566.

804 ——, and ——, 2013: Seasonal and long-term coupling between wintertime storm tracks and
805 sea surface temperature in the North Pacific. *J. Climate*, **26**, 6123–6136.

806 Hoskins, B. J., and K. I. Hodges, 2002: New perspectives on the northern hemisphere winter
807 storm tracks. *J. Atmos. Sci.*, **59**, 1041–1061.

808 ——, I. N. James, and G. H. White, 1983: The shape, propagation and mean-flow interaction
809 of large-scale weather systems. *J. Atmos. Sci.*, **40**, 1595–1612.

810 Hurrell, J. W., and C. Deser, 2009: North Atlantic climate variability: The role of the North
811 Atlantic Oscillation. *J. Mar. Syst.*, **78**, No. 1, 28-41.

812 Joyce, T. M., Y.-O. Kwon, and L. Yu, 2009: On the relationship between synoptic wintertime
813 atmospheric variability and path shifts in the Gulf Stream and the Kuroshio Extension.
814 *J. Climate*, **22**, 3177–3192.

815 Isoguchi O., H. Kawamura and E. Oka, 2006: Quasi-stationary jets transporting surface warm
816 waters across the transition zone between the subtropical and the subarctic gyres in the
817 North Pacific. *J. Geophys. Res*. 111, C10003.
818
819 Kalnay, E., and Coauthors, 1996: The NCEP/NCAR 40-Year Reanalysis Project. *Bull. Amer.*
820 *Meteor. Soc.* , **77**, 437–471.

821 Kelly, K. A., R. J. Small, R. M. Samelson, B. Qiu, T. M. Joyce, Y.-O. Kwon, and M. F.
822 Cronin, 2010: Western boundary currents and frontal air–sea interaction: Gulf Stream
823 and Kuroshio Extension. *J. Climate*, **23**, 5644–5667.

824 Kushnir,Y., W. A. Robinson, I. Bladé, N. M. J. Hall, S. Peng, and R. Sutton, 2002:
825 Atmospheric GCM response to extratropical SST anomalies: synthesis and

826 evaluation*. *J. Climate*, **15**, 2233–2256.

827 Kwon, Y.-O., and T. M. Joyce, 2013: Northern hemisphere winter atmospheric transient eddy
828 heat fluxes and the Gulf Stream and Kuroshio-Oyashio Extension variability. *J.*
829 *Climate*, **23**, 9839-9859.

830 ——, M. A. Alexander, N. A. Bond, C. Frankignoul, H. Nakamura, B. Qiu, and L. A.
831 Thompson, 2010: Role of the Gulf Stream and Kuroshio–Oyashio systems in large-
832 scale atmosphere–ocean interaction: A Review. *J. Climate*, **26**, 3249–3281.

833 Liu, Q., N. Wen, and Z. Liu, 2006: An observational study of the impact of the North Pacific
834 SST on the atmosphere. *Geophys. Res. Lett.*, **33**, L18611.

835 Liu Z., Y. Liu, L. Wu, and R. Jacob, 2007: Seasonal and long-term atmospheric responses to
836 reemerging North Pacific Ocean variability: A combined dynamical and statistical
837 assessment. *J. Climate*, **20**, 955–980.

838 Liu, Z., and L. Wu, 2004: Atmospheric response to North Pacific SST: The role of ocean-
839 atmosphere coupling. *J. Climate*, **17**, 1859-1882.

840 Masunaga, R., H. Nakamura, T. Miyasaka, K. Nishii, and Y. Tanimoto, 2015: Separation of
841 climatological imprints of the Kuroshio Extension and Oyashio fronts on the
842 wintertime atmospheric boundary layer: their sensitivity to SST resolution prescribed
843 for atmospheric reanalysis. *J. Climate*, **28**, 1764–1787.

844 Minobe, S., M. Miyashita, A. Kuwano-Yoshida, H. Tokinaga, and S.-P. Xie, 2010:
845 Atmospheric response to the Gulf Stream: seasonal variations*. *J. Climate*, **23**, 3699–
846 3719.

847 Miyasaka, T., H. Nakamura, B. Taguchi, and M. Nonaka, 2014: Multidecadal modulations of

the low-frequency climate variability in the wintertime North Pacific since 1950. *Geophys. Res. Lett.*, **41**, 2948–2955.

Nakamura, and T. Yamagata, 1999: Recent decadal SST variability in the northwestern Pacific and associated atmospheric anomalies. *Beyond El Niño: Decadal and Interdecadal Climate Variability*, A. Navarra Ed., Springer, 49–72.

——, T. Izumi, and T. Sampe, 2002: Interannual and decadal modulations recently observed in the Pacific storm track activity and East Asian winter monsoon. *J. Climate*, 15, 1855–1874.

——, H., T. Sampe, Y. Tanimoto, and A. Shimpo, 2004: Observed associations among storm tracks, jet streams and midlatitude oceanic fronts. *Earth Climate : The Ocean-Atmosphere Interaction*, G*eophys. Monogr.,* Vol. 147, Amer. Geophys. Union, 329–346.

Nishii, K., H. Nakamura, and Y. J. Orsolini, 2010: Cooling of the wintertime Arctic stratosphere induced by the western Pacific teleconnecion pattern, *Geophys. Res. Lett*, **37**, L13805.

Nonaka, M., H. Nakamura, Y. Tanimoto, T. Kagimoto, and H. Sasaki, 2006: Decadal variability in the Kuroshio-Oyashio Extension simulated in an eddy-resolving OGCM. *J. Climate*, **19**, 1970–1989.

——, ——, ——, ——, and ——, 2008: Interannual-to-decadal variability in the Oyashio and its influence on temperature in the subarctic frontal zone: an eddy-resolving OGCM simulation. *J. Climate*, **21**, 6283–6303.

871 Okajima, S., H. Nakamura, K. Nishii, T. Miyasaka, and A. Kuwano-Yoshida, 2014:
872 Assessing the importance of prominent warm SST anomalies over the midlatitude
873 North Pacific in forcing large-scale atmospheric anomalies during 2011 summer and
874 autumn. *J. Climate*, **27**, 3889–3903.

875 O'Reilly, C. H., and A. Czaja, 2014: The response of the Pacific storm track and atmospheric
876 circulation to Kuroshio Extension variability: response of storm tracks to Kuroshio
877 Extension variability. *Quart. J. Roy. Meteor. Soc.*.

878 Park, S., C. Deser, and M. A. Alexander, 2005: Estimation of the surface heat flux response to
879 sea surface temperature anomalies over the global oceans. *J. Climate*, **18**, 4582–4599.

880 Plumb, R., 1985: On the Three-Dimensional Propagation of Stationary Waves. *J. Atmos. Sci.*,
881 **42**, 217–229.

882 Peng S. and J. S. Whitaker, 1999: Mechanisms determining the atmospheric response to
883 midlatitude SST anomalies. *J. Climate*, **12**, 1393–1408.

884 Polvani, L. M., and D. W. Waugh, 2004: Upward wave activity flux as a precursor to extreme
885 stratospheric events and subsequent anomalous surface weather regimes. *J. Climate*,
886 **17**, 3548–3554.

887 Qiu, B., 2002: Large-scale variability in the midlatitude subtropical and subpolar North
888 Pacific Ocean: observations and causes. *J. Phys. Oceanogr.* , **32**, 353–375.

889 ——, 2003: Kuroshio Extension variability and forcing of the Pacific decadal oscillations:
890 responses and potential feedback. *J. Phys. Oceanogr.* , **33**, 2465–2482.

891 ——, and S. Chen, 2005: Variability of the Kuroshio Extension jet, recirculation gyre, and
892 mesoscale eddies on decadal time scales. *J. Phys. Oceanogr.* , **35**, 2090–2103.

893 ——, and ——, 2010: Eddy-mean flow interaction in the decadally modulating Kuroshio
894 Extension system. *Deep-Sea Res. II*, **57**, 1097–1110.

895 ——, ——, N. Schneider, and B. Taguchi, 2014: A coupled decadal prediction of the
896 dynamic state of the Kuroshio Extension system. *J. Climate*, **27**, 1751–1764.

897 Rivière, G., 2009: Effect of latitudinal variations in low-level baroclinicity on eddy life cycles
898 and upper-tropospheric wave-breaking processes. *J. Atmos. Sci.*, **66**, 1569–1592.

899 Sasaki, Y. N., S. Minobe, and N. Schneider, 2013: Decadal response of the Kuroshio
900 Extension jet to Rossby waves: observation and thin-jet theory*. *J. Phys. Oceanogr.* ,
901 **43**, 442–456.

902 Schneider, N., A. J. Miller, and D. W. Pierce, 2002: Anatomy of North Pacific decadal
903 variability. *J. Climate*, **15**, 586–605.

904 Seager, R., Y. Kushnir, N. H. Naik, M. A. Cane, and J. Miller, 2001: Wind-driven shifts in
905 the latitude of the Kuroshio-Oyashio Extension and generation of SST anomalies on
906 decadal timescales*. *J. Climate*, **14**, 4249–4265.

907 Seo, Y., S. Sugimoto, and K. Hanawa, 2014: Long-term variations of the Kuroshio Extension
908 path in winter: meridional movement and path state change. *J. Climate*, **27**, 5929–
909 5940.

910 Sheldon, L. and A. Czaja, 2014 : Seasonal and interannual variability of an index of deep
911 atmospheric convection over western boundary currents. *Quart. J. Roy. Meteor. Soc.*,
912 140: 22–30.

913 Smirnov, D., M. Newman, and M. A. Alexander, Y.-O. Kwon and C. Frankignoul, 2015:
914 Investigating the local atmospheric response to a realistic shift in the Oyashio sea

915 surface temperature front. *J. Climate*, **28,** 1126–1147.

916 Storch, H. v, and F. W. Zwiers, 1999: *Statistical Analysis in Climate Research*. Cambridge
917 University Press, 484 pp.

918 Sugimoto, S., and K. Hanawa, 2011: Roles of SST anomalies on the wintertime turbulent heat
919 fluxes in the Kuroshio–Oyashio confluence region: influences of warm eddies
920 detached from the Kuroshio Extension. *J. Climate*, **24**, 6551–6561.

921 ——, 2014: Influence of SST anomalies on winter turbulent heat fluxes in the eastern
922 Kuroshio–Oyashio confluence region. *J. Climate*, **27**, 9349–9358.

923 Taguchi, B., S.-P. Xie, N. Schneider, M. Nonaka, H. Sasaki, and Y. Sasai, 2007: Decadal
924 variability of the Kuroshio Extension: observations and an eddy-resolving model
925 hindcast*. *J. Climate*, **20**, 2357–2377.

926 ——, H. Nakamura, M. Nonaka, and S.-P. Xie, 2009: Influences of the Kuroshio/Oyashio
927 Extensions on air–sea heat exchanges and storm-track activity as revealed in regional
928 atmospheric model simulations for the 2003/04 Cold Season*. *J. Climate*, **22**, 6536–
929 6560.

930 ——, ——, ——, N. Komori, A. Kuwano-Yoshida, K. Takaya, and A. Goto, 2012: Seasonal
931 evolutions of atmospheric response to decadal SST anomalies in the North Pacific
932 subarctic frontal zone: observations and a coupled model simulation. *J. Climate*, **25**,
933 111–139.

934 Takaya, K., and H. Nakamura, 2001: A formulation of a phase-independent wave-activity
935 flux for stationary and migratory quasigeostrophic eddies on a zonally varying basic
936 flow. *J. Atmos. Sci.*, **58**, 608–627.

937 Trenberth, K. E., and J. W. Hurrell, 1994: Decadal atmosphere-ocean variations in the Pacific.
938 *Climate Dyn.*, **9**, 303–319.

939 Vivier, F., K. A. Kelly, and L. A. Thompson, 2002: Heat budget in the Kuroshio Extension
940 region: 1993–99. *J. Phys. Oceanogr.* , **32**, 3436–3454.

941 Wagawa, T., Ito S.-I., Shimizu, Y., Kakehi, S., and Ambe, D., 2014: Currents associated with
942 the quasi-stationary jet separated from the Kuroshio Extension. *J. Phys. Oceanogr.*,
943 **44**, 1636–1653.

944 Wen, N., Z. Liu, Q. Liu, and C. Frankignoul, 2010: Observed atmospheric responses to global
945 SST variability modes: A unified assessment using GEFA*. *J. Climate*, **23**, 1739–
946 1759.

947 Yoshiike, S., and R. Kawamura, 2009: Influence of wintertime large-scale circulation on the
948 explosively developing cyclones over the western North Pacific and their downstream
949 effects. *J. Geophys. Res.*, 114, D13110.

950

951 Yu, L., and R. A. Weller, 2007: Objectively analyzed air–sea heat fluxes for the global ice-
952 free oceans (1981–2005). *Bull. Amer. Meteor. Soc.*, **88**, 527–539.

953

954

955 *Figure Captions*
956

957 Fig. 1. Monthly KE index time series before (cyan) and after (blue) cubic trend removal, and
958 after ENSO filtering (orange) (see text) and OE index (thin grey) defined by the leading
959 principal component of the latitude of the maximum meridional SST gradient between 145°

960 and 170°E (Frankignoul et al. 2011). Dots denote positive (red) and negative (blue) extreme
961 events during the ASON season, as used in the composite analysis.

962 Fig. 2. Lagged regression of the Z250 anomaly onto the KE index 2 months earlier (in m) for
963 seasons of 2 months during the cold season, from September-October (SO) to February-
964 March (FM). Thick black lines denote the mean KE and OE paths defined by the mean
965 latitude of the maximum meridional SSH and SST gradient respectively (KE mean path from
966 Kelly et al. 2010), and thick (thin) black contours indicate 10% (5%) significance. Contour
967 interval is 5 m.

968 Fig. 3. Lagged regressions of (left) sea level pressure (SLP), (middle) Z250, and (right)
969 Ekman pumping (EKMP) anomaly fixed in ONDJ onto the KE index for lags given on the
970 left (in month). Positive (negative) lags mean the KE leads (lags) the atmosphere. Contour
971 intervals are (left) 20 Pa, (middle) 5 m and (right) $1x10^{-7}$ 10^{-7} m/s and red (blue) color
972 shading is for positive (negative) anomaly. Thin (thick) black contours indicate 10% (5%)
973 significance.

974 Fig. 4. Estimated response of (a) the SLP (in Pa) and (b) the Z250 (in m) in ONDJ to the KE
975 index 2 months earlier. Contour intervals are (a) 20 Pa and (b) 5 m. Thick black lines denote
976 the mean KE and OE paths, and thin (thick) black contours indicate 10% (5%) significance.

977 Fig. 5. (a) Estimated response of the SST anomaly in SOND onto the KE index 1 month
978 earlier (in K). (b) Same, but for the meridional SST gradient (in 10^{-3} K/km). (c) Same, but
979 for the net heat flux anomaly onto the KE index 2 months earlier (positive upward, in
980 W/m^2). (d) Same as (c) but for NDJF (estimated response after 3 months). Contour intervals
981 are (a) 0.1 K, (b) $1x10^{-3}$ K/km, (c) and (d) 3 W/m^2. Thick black lines denote the mean KE
982 and OE paths, and thin (thick) black contours indicate 10% (5%) significance.

Fig. 6. Upper panel: Estimated response averaged over 155° - 175°E of the meridional and vertical wind velocity anomaly (vectors, scaling arrow in the upper-left corner: 50 m/s, for the meridional component and 5.10^{-3} Pa/s for the vertical component), of the air temperature (shading, in K, with contour interval of 0.1 K) and of the geopotentiel height (thick black contours) in ONDJ onto the KE index 2 months earlier. Thin (dashed) black contour indicates 5% temperature (geopotential) significance, and black vectors indicate 10% significance. Bottom panel: SST anomaly profile shown in Figure 5a averaged over the same longitude band.

Fig. 7. Estimated response of (a) the Eady growth rate anomaly at 850 hPa (in 10^{-2} day^{-1}), (b) the storm track anomaly at 500 hPa (in m), (c) the meridional transient eddy heat flux anomaly at 850 hPa (in K m/s) and (d) the meridional transient eddy moisture flux anomaly at 850 hPa (in 10^{-4} m/s), in ONDJ onto the KE index 2 months earlier. Contour intervals are (a) $2x10^{-2}$ day^{-1}, (b) 0.5 m, (c) 0.2 K m/s and (d) $1.5x10^{-4}$ m/s. Green contours denote the ONDJ climatology, with contours at (a) 50, 70 and $85x10^{-2}$ day^{-1}, (b) 40, 50 and 60 m, (c) 6, 8, 10 and 12 Km/s, and (d) 30, 40 and $50x10^{-4}$ m/s. Thick black lines denote the mean KE and OE paths, and thin (thick) black contours indicate 10% (5%) significance.

Fig. 8. Estimated response of the geopotential height anomaly at (a,c) 250 hPa and (b,d) 100 hPa (shading, in m, with contour interval of 5 m) in (a,b) ONDJ onto the KE index 2 months earlier, (c,d) NDJF onto the KE index 3 months earlier, and corresponding wave activity flux (green vectors, scaling given on the left for the 250hPa level and on the right for the 100hPa level, in m^2/s^2). Thick black lines denote the mean KE and OE paths, and thin (thick) black contours indicate 10% (5%) significance. For clarity, only 10% significant wave activity flux vectors are plotted, and only every third vectors are plotted equatorward of 60°N

and every fifth ones poleward of 60°N.

Fig. 9. (a) Estimated response of the meridional eddy heat flux v*T* at 100 hPa (in Km/s) in ONDJ onto the KE index 2 months earlier, with contour intervals of 3 Km/s. Thick black lines denote the mean KE and OE paths, and thin (thick) black contours indicate 10% (5%) significance. (b) Climatology and climatology + regression of the zonal-mean eddy heat flux [v*T*] at 100 hPa (in Km/s) in ONDJ onto the KE index 2 months earlier. The dots denote 5% significance.

Fig. 10. Estimated response of (a) the temperature anomaly at 900 hPa (in K) and (b) the snow cover extent (in %) in ONDJ onto the KE index 2 months earlier. Contour intervals are (a) 0.1 K and (b) 2%. Thick black lines in (a) denote the mean KE and OE paths. Thin (thick) black contours indicate 10% (5%) significance.

Fig. 11. Positive (a) and negative (b) composite of the SST anomaly (in K) in SOND for extreme KE events in ASON. (c,d) Same, but for the Eady growth rate at 850 hPa in ONDJ (in 10^{-2} day^{-1}). (e,f) Same, but for the storm track anomaly at 500 hPa in ONDJ (in m). Contour intervals are (a,b) 0.2 K, (c,d) $2x10^{-2}$ day^{-1} and (e,f) 1 m. Green contours denote the ONDJ climatology, with contours at (c,d) 50, 70 and $85x10^{-2}$ day^{-1} , and (e,f) 40, 50 and 60 m. Thick black lines denote the mean KE and OE paths, and thin (thick) black contours indicate 10% (5%) significance.

Fig. 12. Climatology of the meridional SST gradient (in 10^{-3} °C/km) in SOND zonally averaged over 155°E – 175°E (black curve), climatology + positive composite (red curve), and climatology + negative composite (blue curve).

Fig. 13. (a) Composite of the SLP anomaly in ONDJ for positive extreme KE events in

ASON (in Pa). (b) Same as (a) but for Z250 (shading, in m) and the wave activity flux (green vectors, scaling arrow is given on the lower-right corner, in m^2/s^2). (c,d) Same as (a,b) but for negative events. Contour intervals are (a,c) 40 Pa and (b,d) 10 m. Thick black lines denote the mean KE and OE paths, and thin (thick) black contours indicate 10% (5%) significance. For clarity, only 10% significant wave activity flux vectors are plotted, and only every third vectors are plotted equatorward of 60°N and every fifth ones poleward of 60°N.

Fig. 14. Positive (left panel) and negative (right panel) composite averaged over 140°E - 160°W of the air temperature anomaly (shading, in K, contour interval 0.2 K) and the geopotential height (contours, in m) in ONDJ for extreme KE events in ASON, and SST anomaly profile of the corresponding composite averaged over the same longitude band (lower panels).

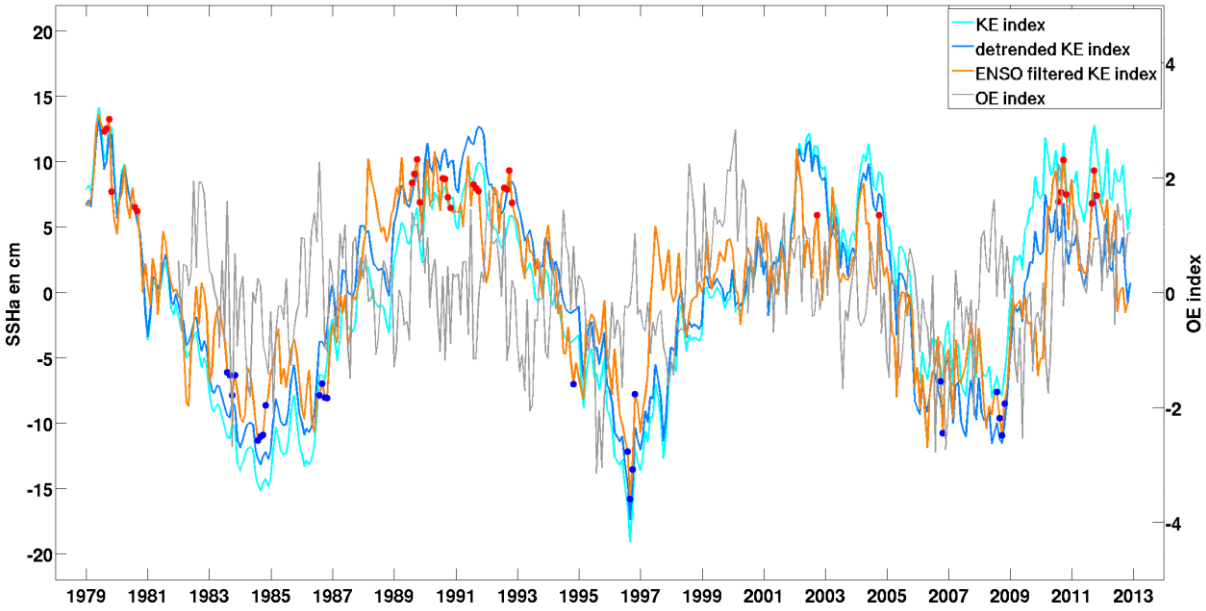

Fig. 1. Monthly KE index time series before (cyan) and after (blue) cubic trend removal, and after ENSO filtering (orange) (see text) and OE index (thin grey) defined by the leading principal component of the latitude of the maximum meridional SST gradient between 145° and 170°E (Frankignoul et al. 2011). Dots denote positive (red) and negative (blue) extreme events during the ASON season, as used in the composite analysis.

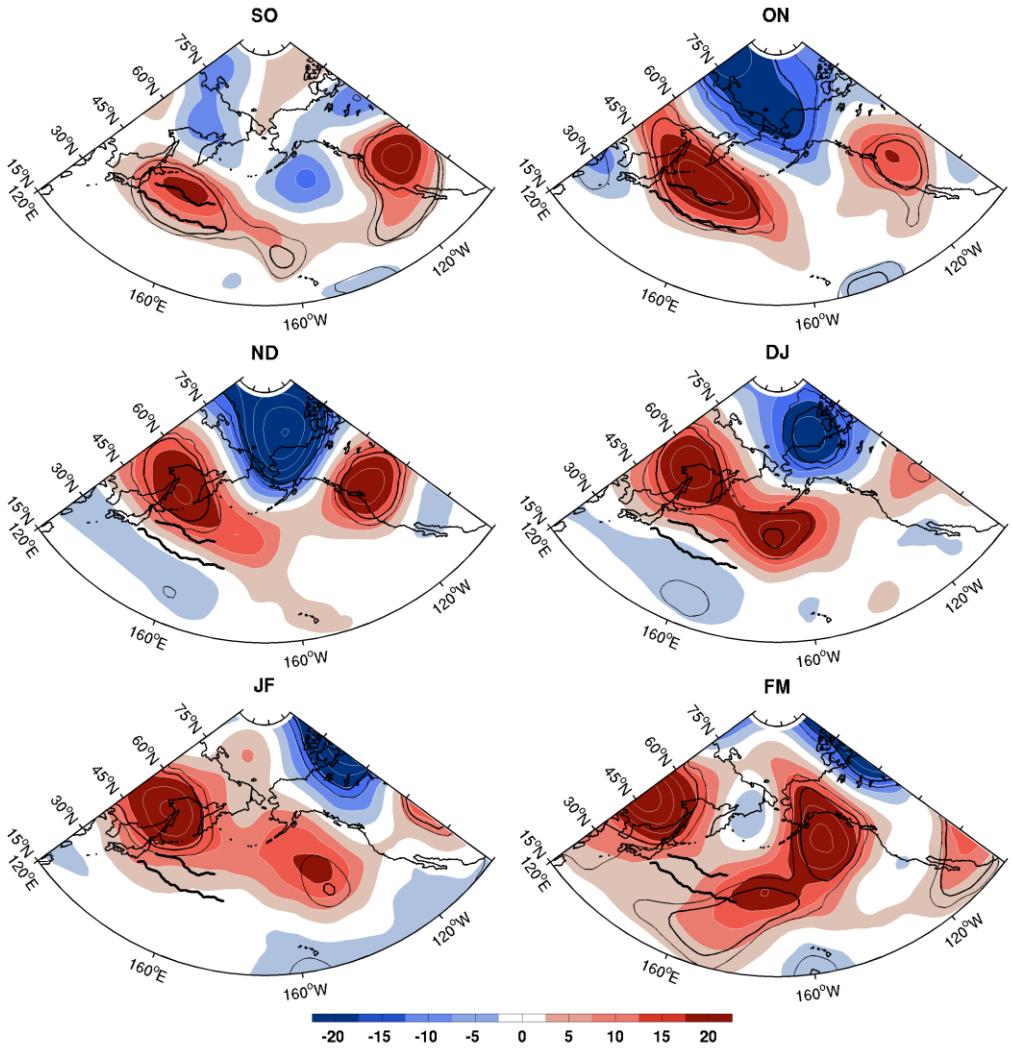

Fig. 2. Lagged regression of the Z250 anomaly onto the KE index 2 months earlier (in m) for seasons of 2 months during the cold season, from September-October (SO) to February-March (FM). Thick black lines denote the mean KE and OE paths defined by the mean latitude of the maximum meridional SSH and SST gradient respectively (KE mean path from Kelly et al. 2010), and thick (thin) black contours indicate 10% (5%) significance. Contour interval is 5 m.

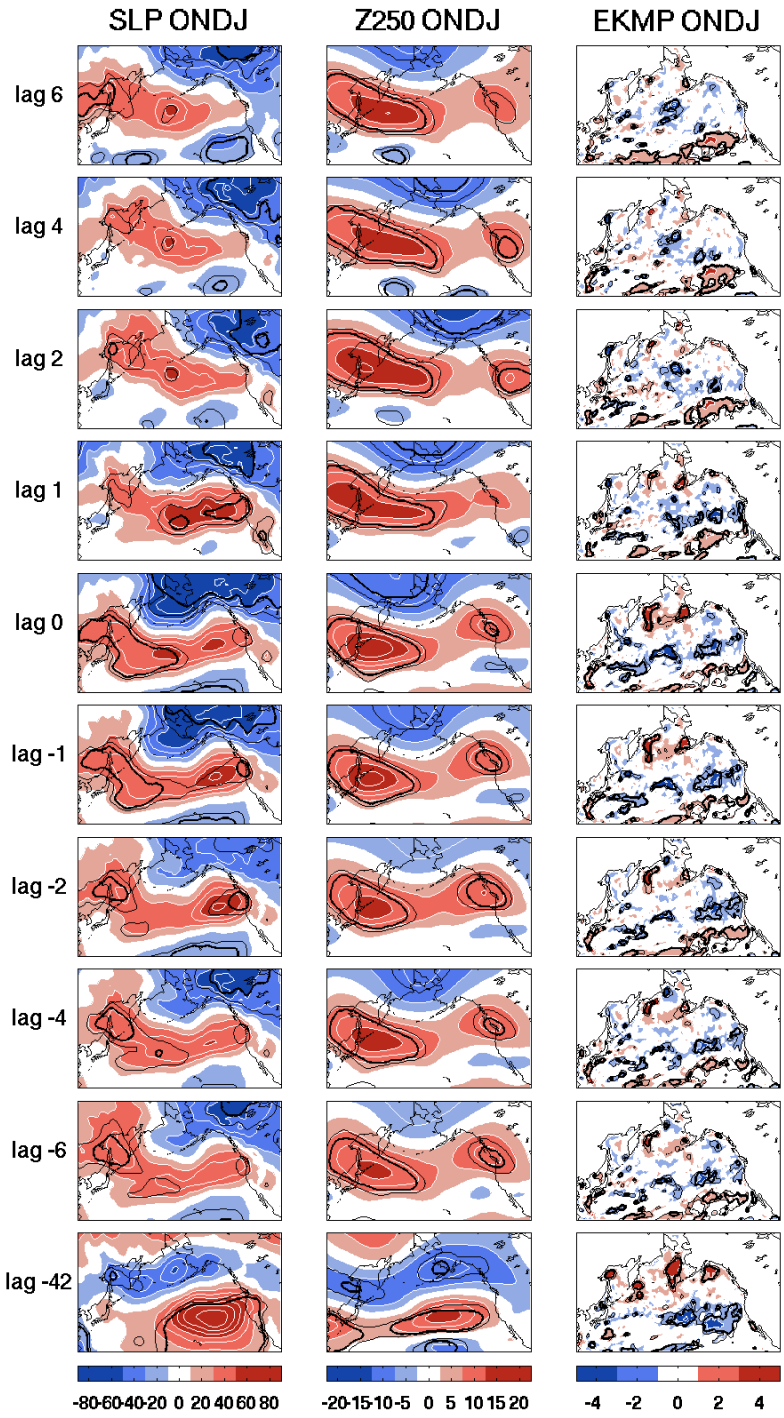

Fig. 3. Lagged regressions of (left) sea level pressure (SLP), (middle) Z250, and (right) Ekman pumping (EKMP) anomaly fixed in ONDJ onto the KE index for lags given on the left (in month). Positive (negative) lags mean the KE leads (lags) the atmosphere. Contour intervals are (left) 20 Pa, (middle) 5 m and (right) 1×10^{-7} m/s and red (blue) color shading is for positive (negative) anomaly. Thin (thick) black contours indicate 10% (5%) significance.

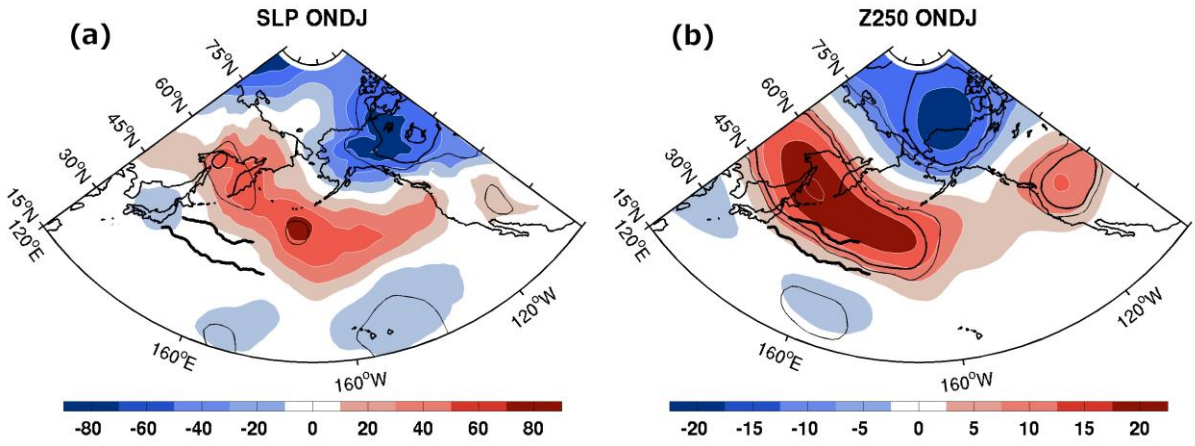

Fig. 4. Estimated response of (a) the SLP (in Pa) and (b) the Z250 (in m) in ONDJ to the KE index 2 months earlier. Contour intervals are (a) 20 Pa and (b) 5 m. Thick black lines denote the mean KE and OE paths, and thin (thick) black contours indicate 10% (5%) significance.

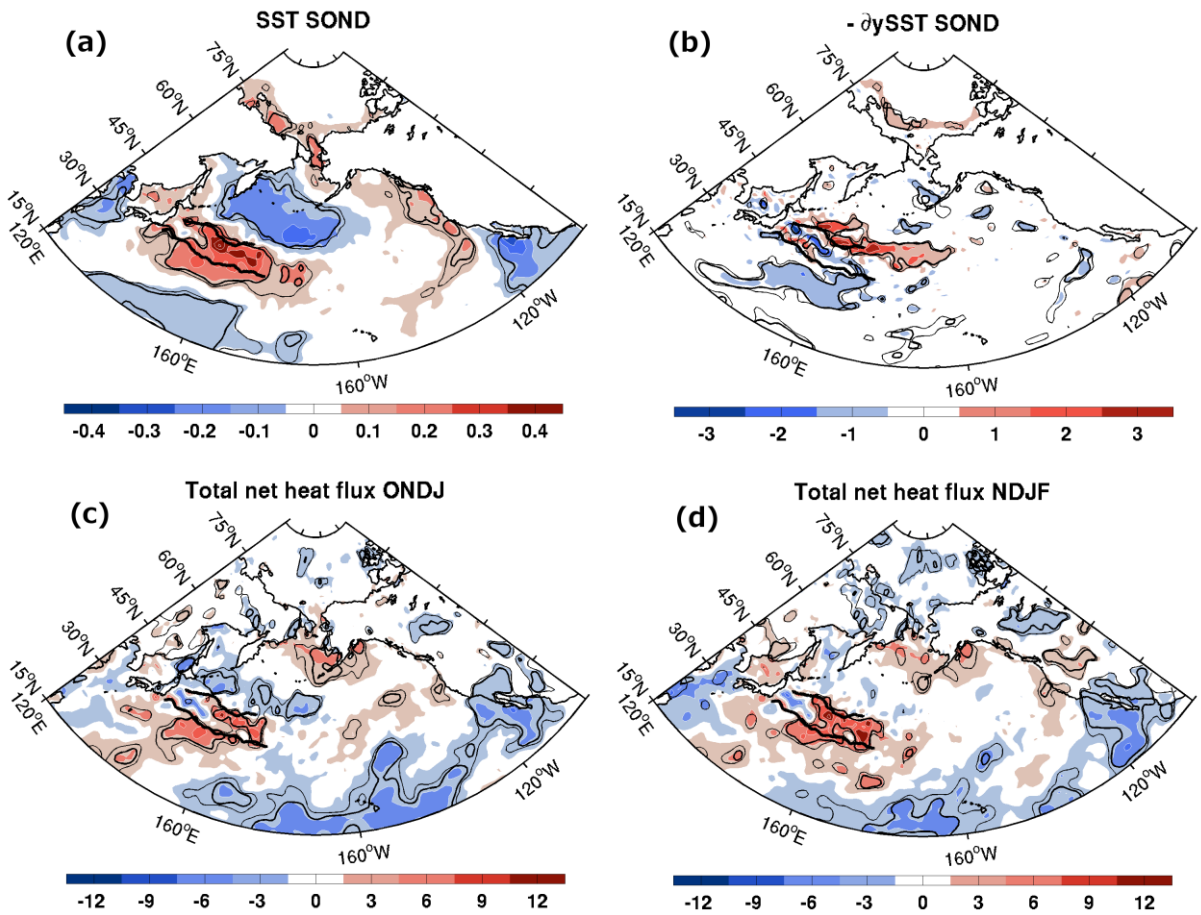

Fig. 5. (a) Estimated response of the SST anomaly in SOND onto the KE index 1 month earlier (in K). (b) Same, but for the meridional SST gradient (in 10^{-3} K/km). (c) Same, but for the net heat flux anomaly onto the KE index 2 months earlier (positive upward, in W/m^2). (d) Same as (c) but for NDJF (estimated response after 3 months). Contour intervals are (a) 0.1 K, (b) $1x10^{-3}$ K/km, (c) and (d) 3 W/m^2. Thick black lines denote the mean KE and OE paths, and thin (thick) black contours indicate 10% (5%) significance.

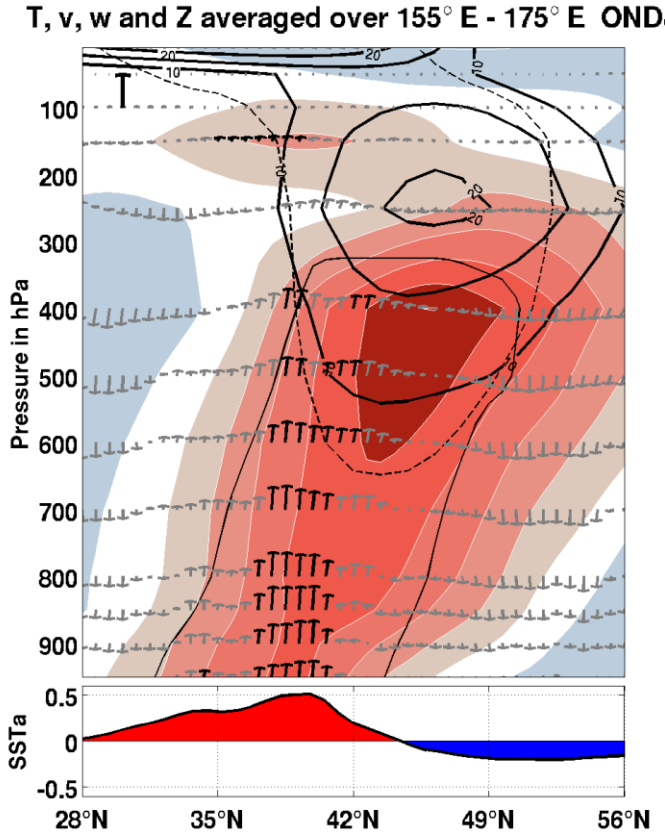

Fig. 6. Upper panel: Estimated response averaged over 155° - 175°E of the meridional and vertical wind velocity anomaly (vectors, scaling arrow in the upper-left corner: 50 m/s, for the meridional component and 5.10^{-3} Pa/s for the vertical component), of the air temperature (shading, in K, with contour interval of 0.1 K) and of the geopotentiel height (thick black contours) in ONDJ onto the KE index 2 months earlier. Thin (dashed) black contour indicates 5% temperature (geopotential) significance, and black vectors indicate 10% significance. Bottom panel: SST anomaly profile shown in Figure 5a averaged over the same longitude band.

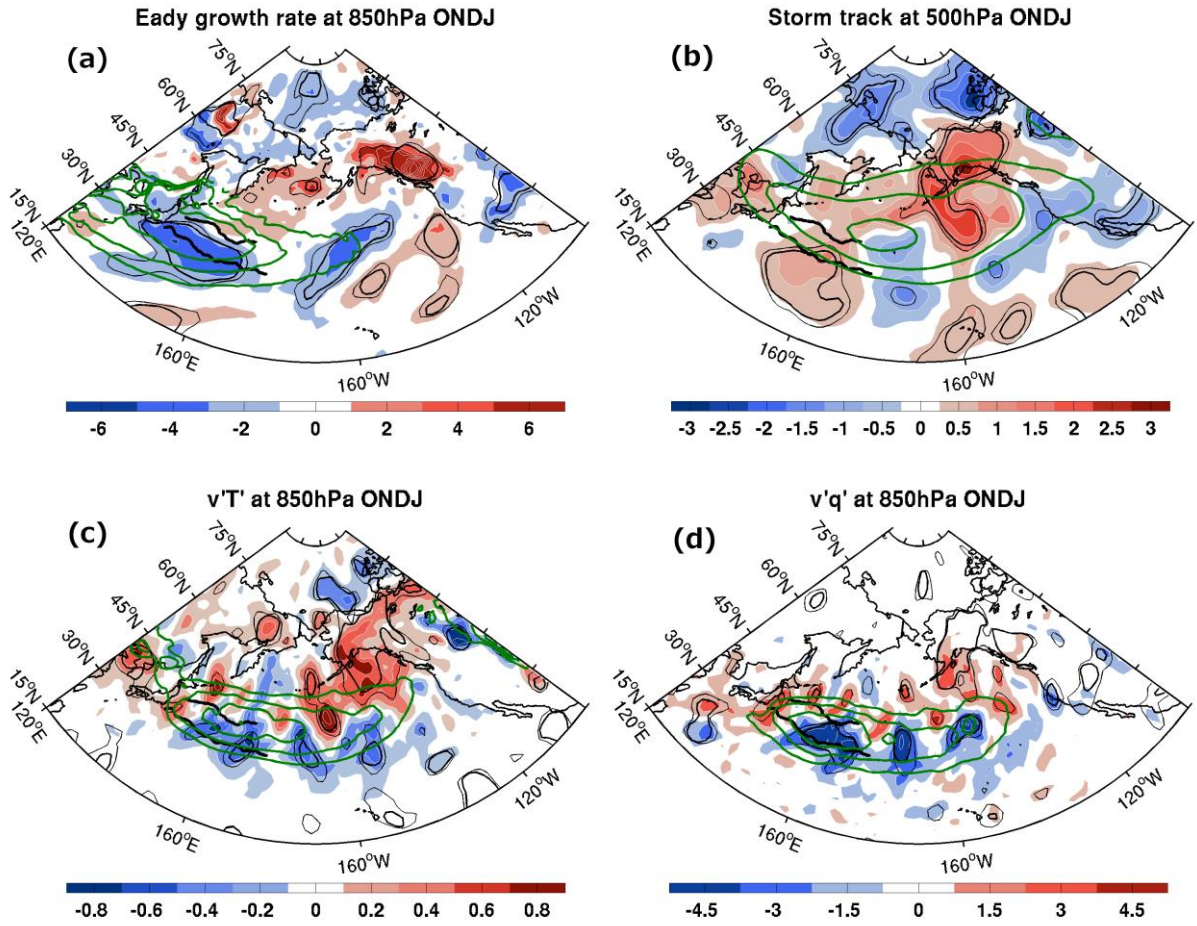

Fig. 7. Estimated response of (a) the Eady growth rate anomaly at 850 hPa (in 10^{-2} day^{-1}), (b) the storm track anomaly at 500 hPa (in m), (c) the meridional transient eddy heat flux anomaly at 850 hPa (in K m/s) and (d) the meridional transient eddy moisture flux anomaly at 850 hPa (in 10^{-4} m/s), in ONDJ onto the KE index 2 months earlier. Contour intervals are (a) $2x10^{-2}$ day^{-1}, (b) 0.5 m, (c) 0.2 K m/s and (d) $1.5x10^{-4}$ m/s. Green contours denote the ONDJ climatology, with contours at (a) 50, 70 and $85x10^{-2}$ day^{-1}, (b) 40, 50 and 60 m, (c) 6, 8, 10 and 12 Km/s, and (d) 30, 40 and $50x10^{-4}$ m/s. Thick black lines denote the mean KE and OE paths, and thin (thick) black contours indicate 10% (5%) significance.

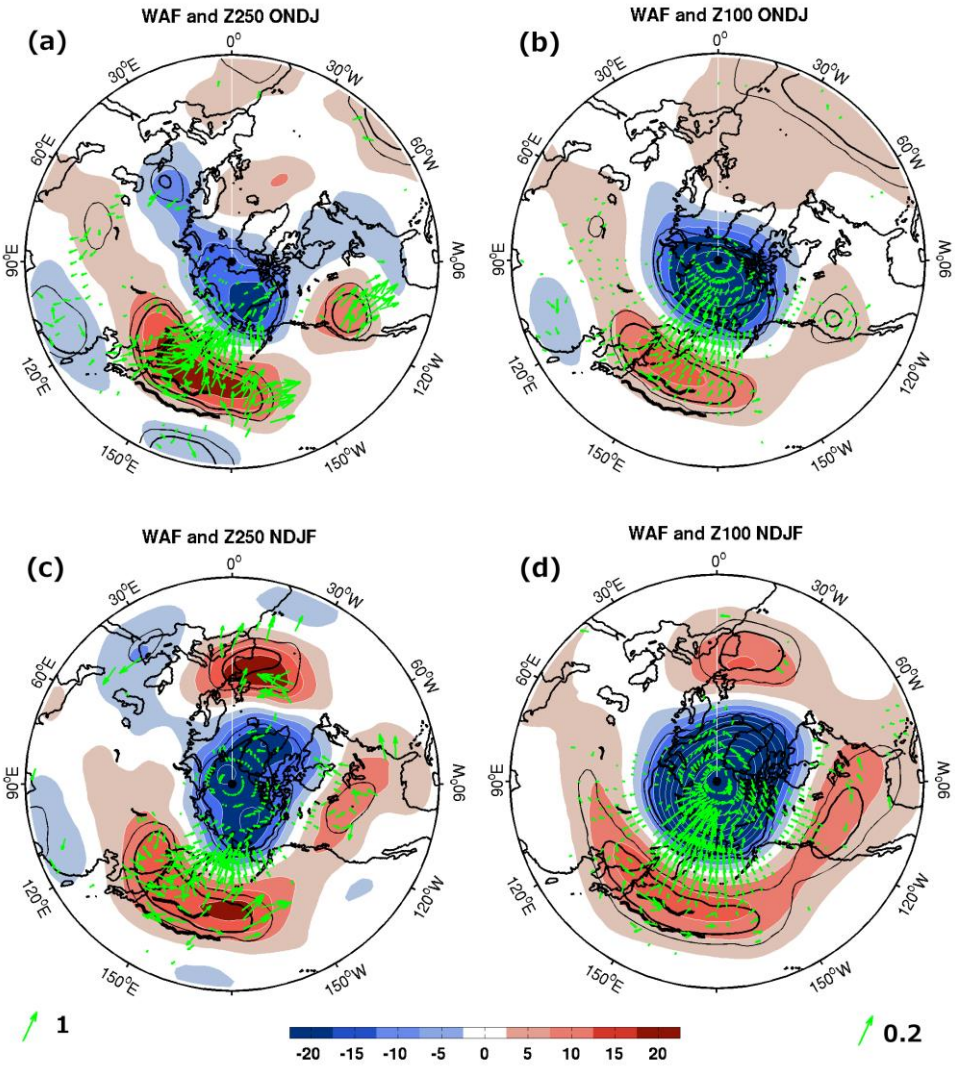

Fig. 8. Estimated response of the geopotential height anomaly at (a,c) 250 hPa and (b,d) 100 hPa (shading, in m, with contour interval of 5 m) in (a,b) ONDJ onto the KE index 2 months earlier, (c,d) NDJF onto the KE index 3 months earlier, and corresponding wave activity flux (green vectors, scaling given on the left for the 250hPa level and on the right for the 100hPa level, in m^2/s^2). Thick black lines denote the mean KE and OE paths, and thin (thick) black contours indicate 10% (5%) significance. For clarity, only 10% significant wave activity flux vectors are plotted, and only every third vectors are plotted equatorward of 60°N and every fifth ones poleward of 60°N.

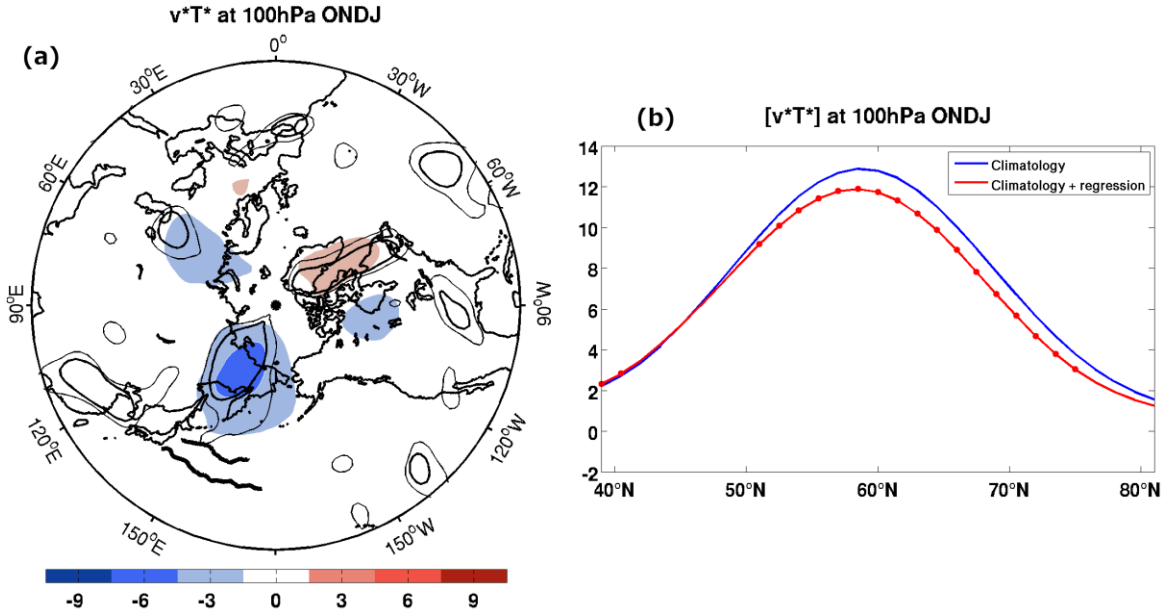

Fig. 9. (a) Estimated response of the meridional eddy heat flux v*T* at 100 hPa (in Km/s) in ONDJ onto the KE index 2 months earlier, with contour intervals of 3 Km/s. Thick black lines denote the mean KE and OE paths, and thin (thick) black contours indicate 10% (5%) significance. (b) Climatology and climatology + regression of the zonal-mean eddy heat flux [v*T*] at 100 hPa (in Km/s) in ONDJ onto the KE index 2 months earlier. The dots denote 5% significance.

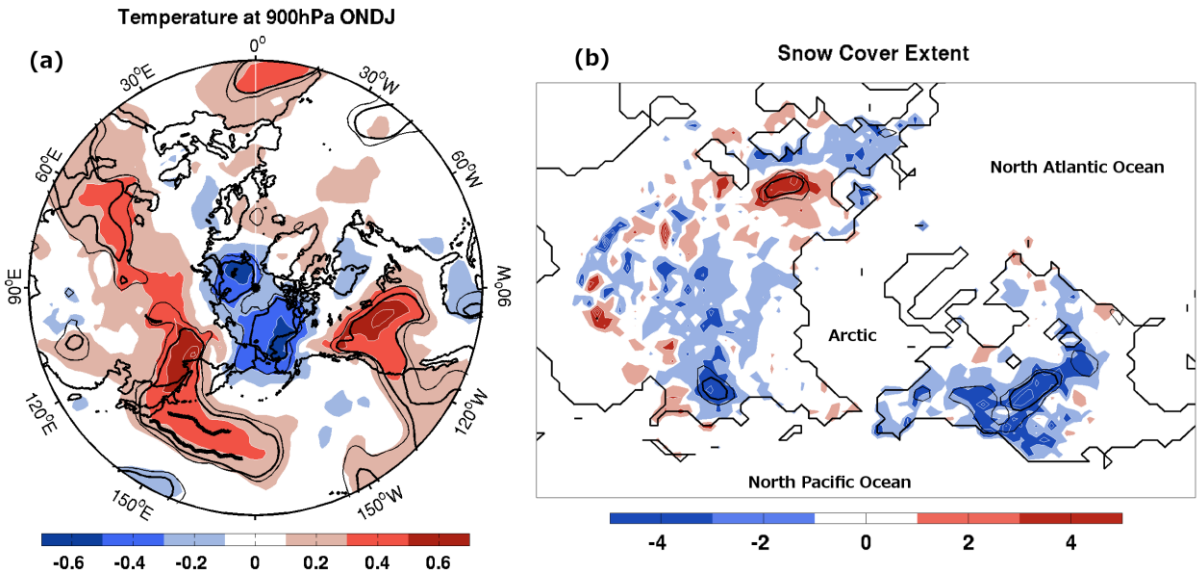

Fig. 10. Estimated response of (a) the temperature anomaly at 900 hPa (in K) and (b) the snow cover extent (in %) in ONDJ onto the KE index 2 months earlier. Contour intervals are (a) 0.1 K and (b) 2%. Thick black lines in (a) denote the mean KE and OE paths. Thin (thick) black contours indicate 10% (5%) significance.

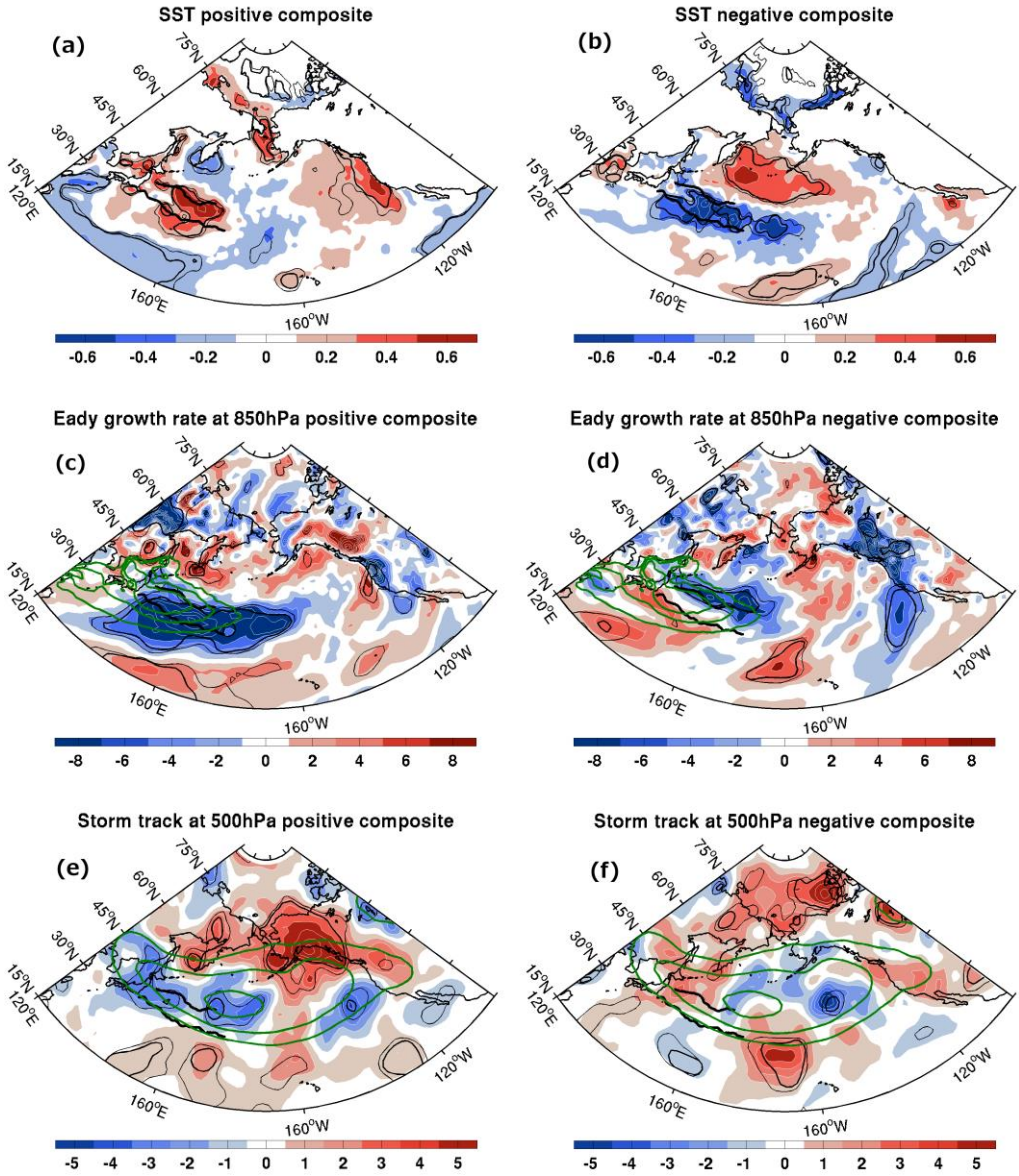

Fig. 11. Positive (a) and negative (b) composite of the SST anomaly (in K) in SOND for extreme KE events in ASON. (c,d) Same, but for the Eady growth rate at 850 hPa in ONDJ (in 10^{-2} day^{-1}). (e,f) Same, but for the storm track anomaly at 500 hPa in ONDJ (in m). Contour intervals are (a,b) 0.2 K, (c,d) 2x10^{-2} day^{-1} and (e,f) 1 m. Green contours denote the ONDJ climatology, with contours at (c,d) 50, 70 and 85x10^{-2} day^{-1} , and (e,f) 40, 50 and 60 m. Thick black lines denote the mean KE and OE paths, and thin (thick) black contours indicate 10% (5%) significance.

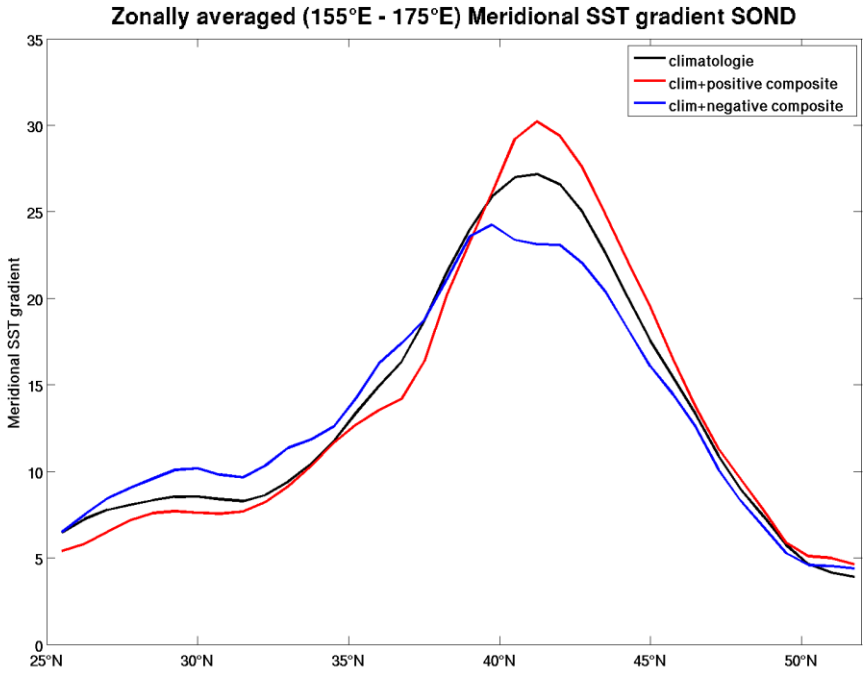

Fig. 12. Climatology of the meridional SST gradient (in 10^{-3} °C/km) in SOND zonally averaged over 155°E – 175°E (black curve), climatology + positive composite (red curve), and climatology + negative composite (blue curve).

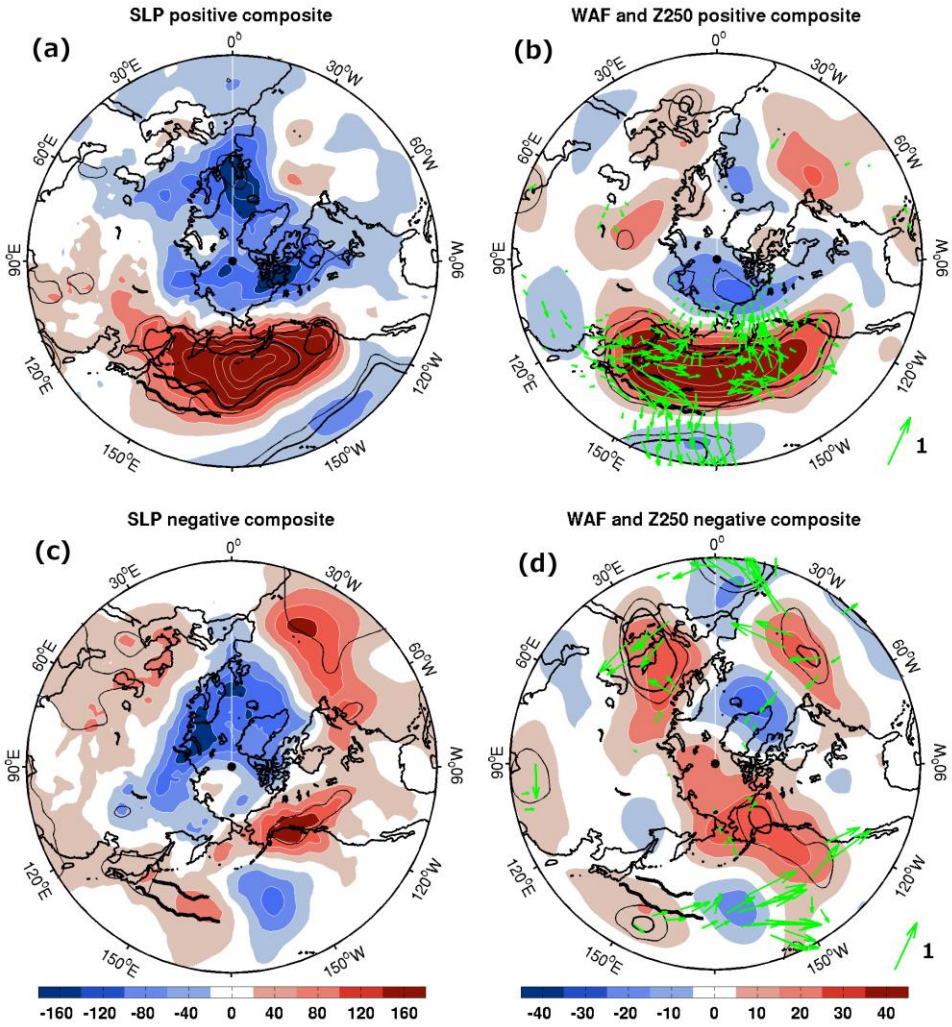

Fig. 13. (a) Composite of the SLP anomaly in ONDJ for positive extreme KE events in ASON (in Pa). (b) Same as (a) but for Z250 (shading, in m) and the wave activity flux (green vectors, scaling arrow is given on the lower-right corner, in m^2/s^2). (c,d) Same as (a,b) but for negative events. Contour intervals are (a,c) 40 Pa and (b,d) 10 m. Thick black lines denote the mean KE and OE paths, and thin (thick) black contours indicate 10% (5%) significance. For clarity, only 10% significant wave activity flux vectors are plotted, and only every third vectors are plotted equatorward of 60°N and every fifth ones poleward of 60°N.

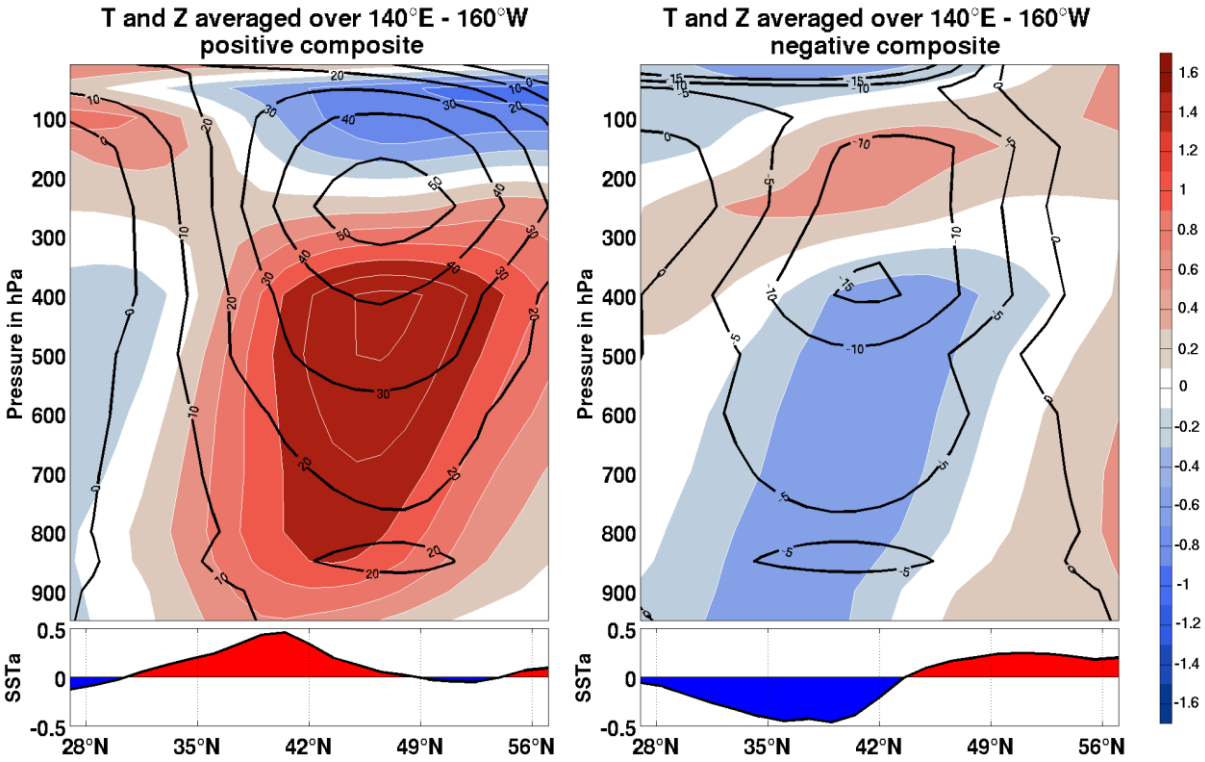

Fig. 14. Positive (left panel) and negative (right panel) composite averaged over 140°E - 160°W of the air temperature anomaly (shading, in K, contour interval 0.2 K) and the geopotential height (contours, in m) in ONDJ for extreme KE events in ASON, and SST anomaly profile of the corresponding composite averaged over the same longitude band (lower panels).